

# Strain accumulation across the Carrizo segment of the San Andreas Fault, California: Impact of laterally varying crustal properties

Gina Schmalzle,<sup>1</sup> Timothy Dixon,<sup>1</sup> Rocco Malservisi,<sup>1,2</sup> and Rob Govers<sup>3</sup>

Received 18 May 2005; revised 29 November 2005; accepted 21 December 2005; published 4 May 2006.

[1] Major strike slip faults juxtapose geologically dissimilar terrain which may vary in mechanical properties, leading to an asymmetric pattern of strain accumulation. We present new GPS data on the Carrizo segment of the San Andreas Fault, separating the Salinian block southwest of the fault from Franciscan terrane northeast of the fault, to better quantify asymmetric strain accumulation. We also present a series of finite element models to investigate the possible role of variable elastic layer thickness and material properties of the upper crust. The geodetic data are well fit with a simple model comprising a weak upper crustal zone 10–25 km wide northeast of the fault. This model is also consistent with geologic data on the distribution of major rock types and corresponding laboratory data on their material properties, as well as paleoseismic, seismic and magnetotelluric data. Using this model, we estimate a “long-term” (average over several seismic cycles) slip rate for the San Andreas Fault of  $36_{-1.5}^{+2}$  mm/yr in agreement with the known Holocene rate within uncertainties, and a viscosity for the combined lower crust/upper mantle of  $2-5 \times 10^{19}$  Pa s.

**Citation:** Schmalzle, G., T. Dixon, R. Malservisi, and R. Govers (2006), Strain accumulation across the Carrizo segment of the San Andreas Fault, California: Impact of laterally varying crustal properties, *J. Geophys. Res.*, *111*, B05403, doi:10.1029/2005JB003843.

## 1. Introduction

[2] Geodetic data near active fault zones can be used to study a variety of fault processes. During the interseismic period, the pattern of surface strain accumulation can be used to estimate the long-term slip rate of the fault [e.g., *Savage and Burford*, 1973; *Lisowski et al.*, 1991] as well as its locking depth and details of the pattern of strain accumulation at depth [e.g., *King et al.*, 1987; *Norabuena et al.*, 2004]. These parameters in turn may be related to the magnitude and pattern of subsequent strain release in the next earthquake. Interseismic geodetic data are therefore an important component of seismic hazard studies. In some cases interseismic geodetic data may also be used to estimate seismic cycle parameters such as earthquake recurrence interval and time since the last earthquake, assuming a simple periodic recurrence model [*Dixon et al.*, 2000; *Segall*, 2002; *Dixon et al.*, 2003].

[3] A necessary condition for such studies is an accurate representation of the mechanical properties (rheology) of the crust and upper mantle. Even if geodetic data fit a given mechanical model, conclusions about fault behavior could be biased if the mechanical properties of the model are

wrong. Most such models assume laterally homogeneous rheology. However, by definition, faults juxtapose different geologic blocks or terrains. For large offset faults, the properties of rocks on opposite sides of the fault can differ significantly. If the contrasts are large enough, these laterally varying properties need to be incorporated in the strain accumulation model [*Rybicki*, 1971; *Rybicki and Kasahara*, 1977; *Hager et al.*, 1999; *Malservisi et al.*, 2001, 2003; *Fay and Humphreys*, 2005; *Le Pichon et al.*, 2005].

[4] *Lisowski et al.* [1991] pointed out that part of the San Andreas Fault (SAF) in central California, separating Franciscan assemblages northeast of the fault from the Salinian block to the southwest (Figures 1 and 2) has a surface deformation profile that is asymmetric, possibly reflecting these contrasting lithologies. In this study, we present new GPS data spanning the Carrizo segment of the SAF, and use these data to better characterize asymmetric surface deformation. We interpret these data in terms of lateral variation of the rheology of upper crustal rocks across the SAF, and use a finite element model to quantify these variations. We show that a model that satisfies the geodetic data is also consistent with independent seismic and magnetotelluric data, as well as paleoseismic data and geologic data on the distribution of major rock types.

## 2. Geologic Setting

[5] The San Andreas Fault (SAF) is a right-lateral strike-slip fault with a strike length of over 1200 km, from northern California to the Gulf of California. Terranes on opposite sides of the fault have been displaced up to

<sup>1</sup>Rosenstiel School of Marine and Atmospheric Sciences, University of Miami, Miami, Florida, USA.

<sup>2</sup>Now at Department of Earth and Environmental Sciences, Ludwig-Maximilians University, Munich, Germany.

<sup>3</sup>Faculty of Earth Sciences, Utrecht University, Utrecht, Netherlands.

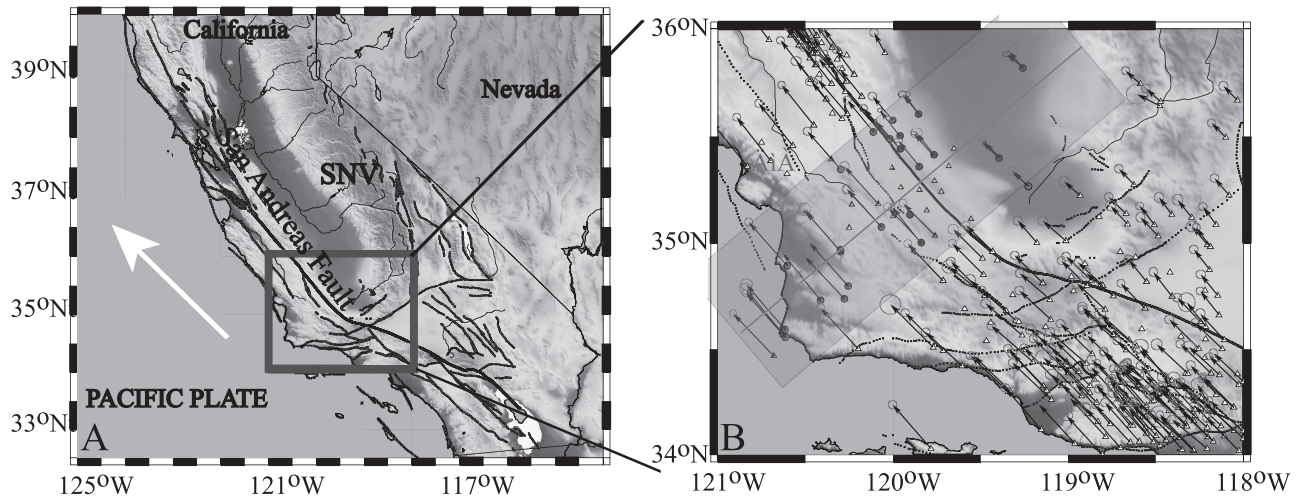


**Figure 1.** (a) Location of study area. Large arrow shows direction of Pacific plate motion relative to stable North America, calculated on the San Andreas Fault at the center of our study area (Figure 1b). SNV is Sierra Nevada block. (b) Enlarged view of the study area and GPS site velocity data from SCEC version 3 velocity field. Arrows tipped with 95% error ellipse indicate direction and magnitude of motion originating from site monument (small dots) relative to stable North America. Shaded rectangle perpendicular to the San Andreas Fault represents location of transect: all data within the rectangle are projected onto the center line in subsequent figures.

~300 km. The fault initiated about 30 Ma and currently accommodates most relative motion between the Pacific and North American plates in California [Crowell, 1952; Atwater, 1970; Powell and Weldon, 1992]. Averaged over the last 3.16 Myr, the total plate motion rate is approximately 48 mm/yr [DeMets and Dixon, 1999], of which ~35 mm/yr occurs on the SAF [Savage and Burford, 1973; Page, 1981; Sieh and Jahns, 1984; Lisowski et al., 1991].

[6] The Carrizo segment of the SAF lies west of the Temblor Range and east of the Carrizo Plain (Figure 2). The southwestern side of the fault is the Salinian block, composed mostly of granitic plutons and metasedimentary rocks of amphibolite and higher metamorphic grades, interpreted as part of a former magmatic arc [Page, 1981]. The northeastern side of the fault is Franciscan terrane and includes both oceanic and terrigenous materials, interpreted as a former subduction zone complex. Coherent units here include Cretaceous sandstone, chert-graywacke sequences and Upper Jurassic chert-greenstone units. The Franciscan also includes mélanges derived from the coherent rock units, together with serpentinite, blueschist and conglomerate [Page, 1981]. Rocks on each side of the fault thus have a strong lithologic contrast.

[7] The Carrizo segment is oriented essentially parallel to the overall plate motion direction and the local direction of Pacific-Sierra Nevada block relative motion (Figure 1a). It lies south of the creeping segment near Parkfield and north of the transpressive Big Bend region (Figures 1 and 2). The fault appears to be fully locked from the surface to seismogenic depths (~10–20 km, Figures 2 and 3), and at least for the last few earthquake cycles, ruptures approximately every 200 years in magnitude 7–8 strike-slip earthquakes [Jackson et al., 1995]. Thus the Carrizo segment approximates a simple model whereby steady far-field plate motion leads to periodic earthquakes, with strain accumulating on the fault during an interseismic period of fixed length, and

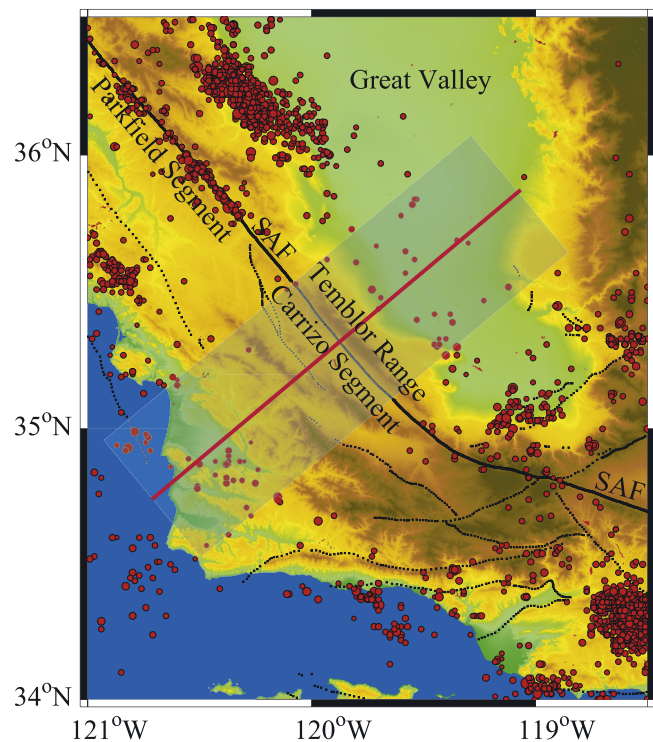


**Figure 2.** Digital elevation model (DEM) and earthquake locations in the study area. DEM is from NASA's Shuttle Radar Topography Mission (SRTM). Earthquake data from U.S. Geological Survey National Earthquake Information Center (NEIC), showing all events larger than magnitude 1.9 for period 1973 to 2004 (total 2210 events). Major segments of San Andreas Fault (SAF; black line) discussed in text are labeled. Note that Carrizo segment is currently aseismic. Study transect represented by translucent blue box and red line.

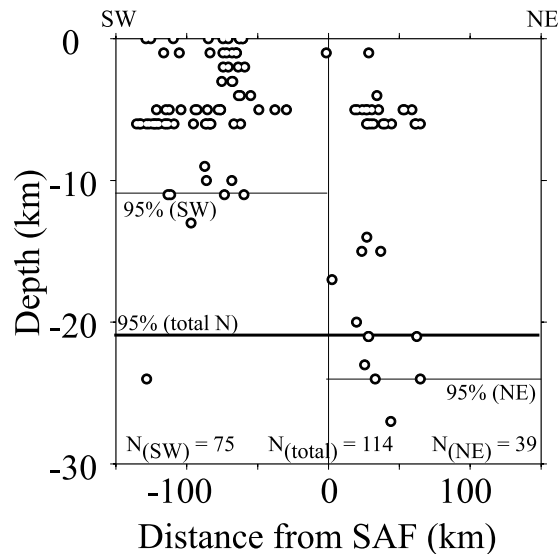


**Figure 3.** Depth distribution of seismicity in study region. NEIC seismicity data (1973–2004, all events) within study area (translucent blue box in Figure 2) are projected onto study transect line. Horizontal lines represent the depth at which 95% of the events are shallower, for events northeast or southwest of San Andreas Fault (light lines) or for all events (heavy line). Seismicity in the study region near the fault is sparse because this segment of the fault is locked.

suddenly released as an earthquake at the end of the cycle. The key parameters in such a model are well constrained by geologic data for the Carrizo segment: the long-term slip rate of the fault ( $34 \pm 3$  mm/yr) [Sieh and Jahns, 1984; Jackson *et al.*, 1995], the earthquake recurrence interval ( $206 + 149/-125$  years) [Jackson *et al.*, 1995], and the date of the last major earthquake (1857 Fort Tejon earthquake) (Table 1a). The Los Alamos Fault,  $\sim 60$  km southwest of the Carrizo segment, has been active in Holocene time and may accommodate several millimeters per year of motion in this region [Jennings and Saucedo, 1994]. The impact of the Los Alamos Fault on the overall strain accumulation pattern is small; we ran models with and without this fault included.

### 3. Data Collection and Analysis

[8] The Southern California Earthquake Center (SCEC) has produced a surface velocity field (SCEC version 3) for much of the southern and central San Andreas region from available Global Positioning System (GPS), electronic distance meter (EDM) and very long baseline interferometry (VLBI) data (Z. K. Shen *et al.*, The SCEC crustal motion map, version 3.0, 2003 available at <http://epicenter.usc.edu/cmm3/>). Data density within the Carrizo segment region is sparse compared to regions to the north and south (Figure 1b). Prior to our work, many sites have not had satisfactory occupation times with GPS since 1994 (Table 2). Velocity uncertainties here are also larger (Table 3) reflecting relatively few observations at a given site.

[9] For this study, we focus on GPS data collected between 1994 and 2003. Since the velocity uncertainty depends on the total number of observations as well as

**Table 1a.** Fault Parameters

	Nominal Value	Tested Values
Rate, mm/yr	$34 \pm 3^{a,b}$	25–50 <sup>c</sup>
Recurrence interval, years	206 (+149/–125) <sup>a</sup>	205 <sup>d</sup>
Last earthquake, years past	142 <sup>d</sup>	150 <sup>d</sup>

<sup>a</sup>Jackson *et al.* [1995].

<sup>b</sup>Sieh and Jahns [1984].

<sup>c</sup>Range of rates tested in case III and IV models.

<sup>d</sup>Time between 1857 earthquake and middle of GPS time series is 142 years. To simplify calculations related to time stepping of finite element model, this is rounded to 150 years. Similarly recurrence interval is set to 205 years.

the total length of the observing period [e.g., Mao *et al.*, 1999], we reoccupied key sites in our study area (shaded rectangle, Figures 1b and 2) in October 2003 in an experiment we call Carrizo 2003. For all sites, this reoccupation extends the time series of GPS data significantly (Table 2). For some sites, our reoccupations allow us to define a GPS site velocity for the first time. The study area is essentially a profile perpendicular to the Carrizo segment (Figures 1b and 2). The 10 Carrizo sites were occupied for a minimum of two complete 24 hour days during the 2003 campaign. Data from this experiment have been archived at UNAVCO (<http://www.unavco.org>) and are publicly available. Table 2 lists the sites used for this study and their occupation times.

[10] Raw GPS files obtained from SCEC and from Carrizo 2003 were analyzed at the University of Miami following Dixon *et al.* [1997] and Sella *et al.* [2002]. We used the GIPSY software developed by the Jet Propulsion Laboratory (JPL) [Zumberge *et al.*, 1997]. The resulting velocities are defined in the IGSA00 global reference frame [Altamimi *et al.*, 2002] (Table 3). Uncertainties are estimated following Mao *et al.* [1999] and Dixon *et al.* [2000], accounting for both white and time-correlated noise (Table 3). A formal inversion procedure [Ward, 1990] is used to derive site velocities relative to stable North America (G. Sella, REVEL-IT00-2003, personal communication, 2003) (Table 3). We use all available post-1993 data for sites within 30 km of the profile shown in Figures 1b and 2. Figure 4 plots the fault-parallel velocity component as a function of perpendicular distance from the fault. Figure 4a shows the SCEC version 3.0 data. Figure 4b shows the updated velocity data for the sites occupied during Carrizo 2003 (for these sites, all GPS data from 1994 and onward were reanalyzed for consistency). For Carrizo 2003 sites where velocities were previously defined, the uncertainties are considerably reduced with incorporation of the new data. Figure 4c shows the velocity profile for

**Table 1b.** Material Parameters

	Nominal Values	Tested Values, Cases I and IVA		Tested Values, Cases II, III, and IVB		
		SW	NE	SW	Weak Zone	NE
Poisson's ratio	0.25	0.25	0.25	0.25	0.25	0.25
Young's modulus, GPa	75 <sup>a</sup>	75	75	50	10–60	75
Elastic layer thickness, km	–	10	5–20	15	15	15
Viscosity, $\times 10^{19}$ Pa s	3–4 <sup>b</sup>	1–6	1–6	1–6	1–6	1–6

<sup>a</sup>Stein and Wysession [2003].

<sup>b</sup>Kenner and Segall [2000, 2003].

**Table 2.** Days of GPS Observation Used in This Study, 1994–2003

Site	Longitude °E	Latitude °N	1994	1996	1998	2000	2001	Carrizo 2003
0504	-119.838	35.003	–	–	2	–	4	2
0611	-118.727	36.185	–	–	4	–	–	–
0613 <sup>a</sup>	-119.259	35.819	2	–	–	–	–	3
7HLI	-120.3	34.96	2	–	–	–	–	5
ALVA	-120.617	34.593	3	–	–	–	–	–
C616	-120.001	35.575	2	–	–	2	–	–
CAUV <sup>a</sup>	-119.394	35.358	2	–	–	–	–	3
FIBR1	-119.394	35.398	3	–	–	–	–	4
GOUD <sup>a</sup>	-119.766	35.414	3	–	–	–	–	4
GRSY	-120.414	34.731	5	–	–	–	–	–
LAMO	-120.257	34.798	4	–	–	–	–	–
LASY	-119.957	35.441	3	–	–	–	–	8
LOSP	-120.606	34.894	4	–	–	–	–	–
MADC	-120.067	35.076	3	–	–	–	–	–
NAPO	-119.959	35.503	3	–	–	–	–	6
ORES <sup>b</sup>	-120.279	34.739	–	–	–	–	–	–
P807 <sup>a</sup>	-119.853	35.603	1	–	–	1	–	3
POSO	-120.113	35.52	10	–	–	2	–	–
RUS1	-120.627	34.571	3	–	–	–	–	–
SAL2	-119.902	35.133	2	–	–	–	–	4
TWR2	-120.018	35.488	–	2	–	–	5	–
VNDP <sup>b</sup>	-120.616	34.556	–	–	–	–	–	–

<sup>a</sup>These sites were affected by strong solar flares on 19 October to 4 November 2003. The only day with data that showed significant effects from these flares was 20 October 2003. These data are not used in this study.

<sup>b</sup>ORES and VNDP are permanent stations. Data are archived at the Scripps Orbit and Permanent Array Center (SOPAC, <http://sopac.ucsd.edu/>).

the combined data sets, i.e., SCEC version 3.0 velocities for sites not occupied in Carrizo 2003; otherwise the updated velocities. Despite minor differences in how the two reference frames are defined, the two data sets are quite consistent. Hereafter, we use only the combined data set.

[11] SCEC vertical data are not publicly available. Vertical data for the Carrizo 2003 sites are listed in Table 3 and show significant subsidence, up to 18 mm/yr. *Fielding et al.* [1998] and *Xu et al.* [2001] use synthetic aperture radar

interferometry to detect subsidence of up to 400 mm/yr near our study region. The rapid subsidence is likely due to active pumping of oil and/or water within the region. We do not use vertical data in this study, and assume that the horizontal data are not affected by subsidence beyond the level of measurement uncertainty. As a test of this assumption, we reran several of our best fit models (e.g., Table 5 in section 5) with a modified data set, eliminating the three data with subsidence rates in excess of 10.0 mm/yr. The parameter

**Table 3.** GPS Velocities and Uncertainties<sup>a</sup>

Site	Velocity SCEC Version 3, mm/yr		Velocity After CARRIZO 2003 (This Study), mm/yr		
	East	North	East	North	Vertical
0504	-27.3 ± 1.4	28.9 ± 1.3	-23.2 ± 2.2	29.3 ± 0.6	-5.6 ± 6.7
0611	-12.3 ± 3.3	11.5 ± 1.8	–	–	–
0613	-12.1 ± 3.2	14.2 ± 3.2	-13.0 ± 0.7	10.8 ± 0.5	-18.4 ± 1.7
7HLI	-29.4 ± 2.2	34.1 ± 2.0	-28.0 ± 0.9	32.2 ± 0.3	-9.5 ± 2.0
ALVA	-31.2 ± 2.0	36.4 ± 1.8	–	–	–
C616	-16.6 ± 1.4	19.5 ± 1.3	–	–	–
CAUV	–	–	-16.8 ± 0.9	20.6 ± 0.3	-6.0 ± 2.4
FIBR	-13.9 ± 1.3	13.2 ± 1.2	-12.6 ± 0.6	11.7 ± 0.2	-11.4 ± 2.8
GOUD	-14.2 ± 1.9	17.5 ± 1.6	-15.9 ± 0.5	17.9 ± 0.4	-7.0 ± 1.0
GRSY	-30.8 ± 1.4	38 ± 1.3	–	–	–
LAMO	-31.3 ± 1.8	35 ± 1.6	–	–	–
LASY	–	–	-19.8 ± 0.4	22.7 ± 0.4	-1.5 ± 1.4
LOSP	-30.9 ± 1.3	35.2 ± 1.3	–	–	–
MADC	-27.6 ± 1.3	30.6 ± 1.3	–	–	–
NAPO	–	–	-16.5 ± 0.9	21.0 ± 0.6	-9.5 ± 2.0
ORES	-31.8 ± 1.4	34 ± 1.4	–	–	–
P807	-13 ± 1.3	15.7 ± 1.2	-12.1 ± 1.0	16.6 ± 0.2	-10.3 ± 1.3
POSO	-21.1 ± 1.3	25.8 ± 1.3	–	–	–
RUS1	-30.3 ± 2.0	36.7 ± 1.8	–	–	–
SAL2	–	–	-27.3 ± 0.6	25.9 ± 0.3	-0.8 ± 1.6
TWR2	-21.4 ± 1.3	24.7 ± 1.2	–	–	–
VNDP	-31.7 ± 1.2	35.6 ± 1.2	–	–	–

<sup>a</sup>Rates and uncertainties are in millimeters per year. Uncertainties for new velocities are calculated following *Dixon et al.* [2000]. Data acquired prior to 1994 are used in SCEC version 3. EDM and VLBI data, also used in the SCEC version 3 data, are not used in our analysis. Sites that were not reoccupied during Carrizo 2003 retain the SCEC version 3 result; other sites have been reanalyzed using the new GPS data. The new result is then incorporated into our final data set. Vertical rates for Carrizo 2003 sites are reported but not used in this study. Fast subsidence rates may be due to oil and/or water pumping in the study region. SCEC version 3 does not report vertical rates. Days of data not listed have high uncertainties due to short observation times and are not included in this study.

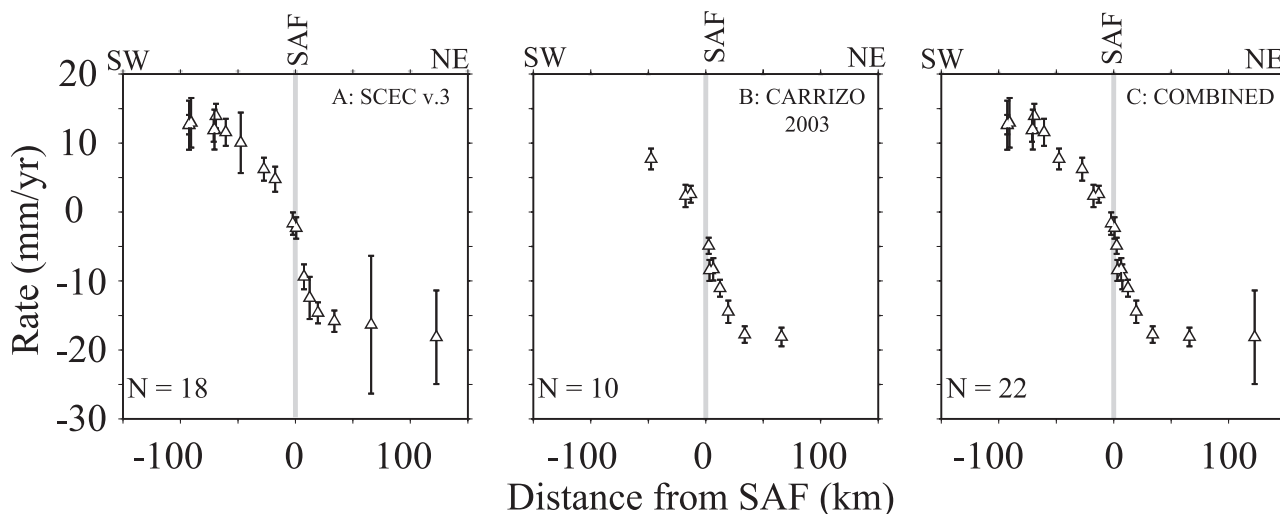


**Figure 4.** (a) GPS velocity profile across study transect, showing all available SCEC version 3 data. (b) New velocity data based on raw SCEC GPS observations from 1994 to 2003 reanalyzed for this study, combined with Carrizo 2003 observations. Sites not reoccupied during the Carrizo 2003 observations are not shown. (c) Combined velocity profile (SCEC version 3 and Carrizo 2003). Sites not occupied during Carrizo 2003 retain SCEC version 3 velocity (Figure 4a); remaining sites use updated velocity (Figure 4b). The combined data set is used for all models discussed in this paper.  $N$  is the number of data.

estimates were virtually identical with those obtained from the full data set, suggesting that “leakage” between the vertical and horizontal components is indeed small.

[12] The site velocities plotted in Figure 1b are relative to stable North America. For the Carrizo segment, the directions of motion would be very similar had we plotted velocities relative to the Sierra Nevada block, although the velocity magnitudes would be reduced by 11–13 mm/yr. The different local reference frames (North America versus Sierra Nevada block) have essentially no impact on the estimated parameters in our fault models, which are mainly sensitive to the velocity gradient across the fault.

#### 4. Symmetric Strain Accumulation Models

[13] We first examine a series of symmetric models to define the magnitude and character of asymmetric strain accumulation. Using simple analytic models combined with an  $F$  test, we demonstrate that models incorporating laterally varying mechanical properties can reduce data misfit significantly. We then use more sophisticated models that explicitly include lateral variation in mechanical properties as constrained by seismic data to test mechanisms that may contribute to asymmetry.

##### 4.1. Simple Elastic Half-Space Model

[14] A simple model for strain accumulation associated with a strike-slip fault is based on a screw dislocation in a uniform elastic half-space [Weertman and Weertman, 1964; Savage and Burford, 1973; Savage, 1980; Lisowski et al., 1991]:

$$v = (v_o/\pi) \arctan(x/D) \quad (1)$$

where  $v$  is the velocity parallel to fault strike,  $x$  is distance from the fault,  $D$  is the dislocation depth (locking depth) interpreted here as equivalent to the elastic layer thickness

in subsequent coupling models, and  $v_o$  is the far-field velocity, usually equated with the long-term slip rate. We solve for the best fit elastic half-space model by varying locking depth and far-field velocity in a simple forward model (grid search) approach, minimizing the  $\chi^2$  misfit function (L2 norm) (Figures 5a and 5b and Table 4a). Uncertainties are estimated using the  $F$  statistic to estimate the  $\chi^2$  misfit corresponding to the 95% confidence level:

$$\chi_{95\%}^2 = \chi_{\text{best}}^2 \{1 + [\nu_1/(\nu_2 - \nu_1)]F\} \quad (2)$$

where  $\chi_{\text{best}}^2$  is the best fit  $\chi^2$ ,  $\nu_1$  is the number of adjustable parameters (two in this example, locking depth and far-field velocity),  $\nu_2$  is the number of data, and  $F$  is the  $F$  statistic computed at  $F_{\nu_1, \nu_2}$ .

[15] As in most such studies, estimates for fault rate and locking depth are correlated, i.e., there is a trade-off between these two parameters, and a range of values fit the data acceptably well (Figure 5a). The best fit model (Table 4a and Figure 5b) systematically misfits numerous data on each side of the fault by about 2–3 mm/yr (Figure 5c), larger than the typical measurement uncertainty,  $\sim 1.0$ – $1.5$  mm/yr at one standard deviation.

[16] An alternate way to assess asymmetric strain accumulation is to fit the data on one side of the fault and inspect for systematic misfit on the other side (Figures 5d–5i and Table 4a). The asymmetric strain accumulation pattern is clear, with higher velocity gradients near the fault on the northeast side compared to the southeast. Thus shallower apparent locking depths provide a better fit northeast of the fault. The maximum asymmetry is about 6 mm/yr, at distances of 18 km from the fault (Figures 5e and 5f, southwestern misfit) or 20 km from the fault (Figures 5h and 5i, northeastern misfit).

[17] Are models that account for this asymmetry warranted in a statistical sense? In other words, is the reduction

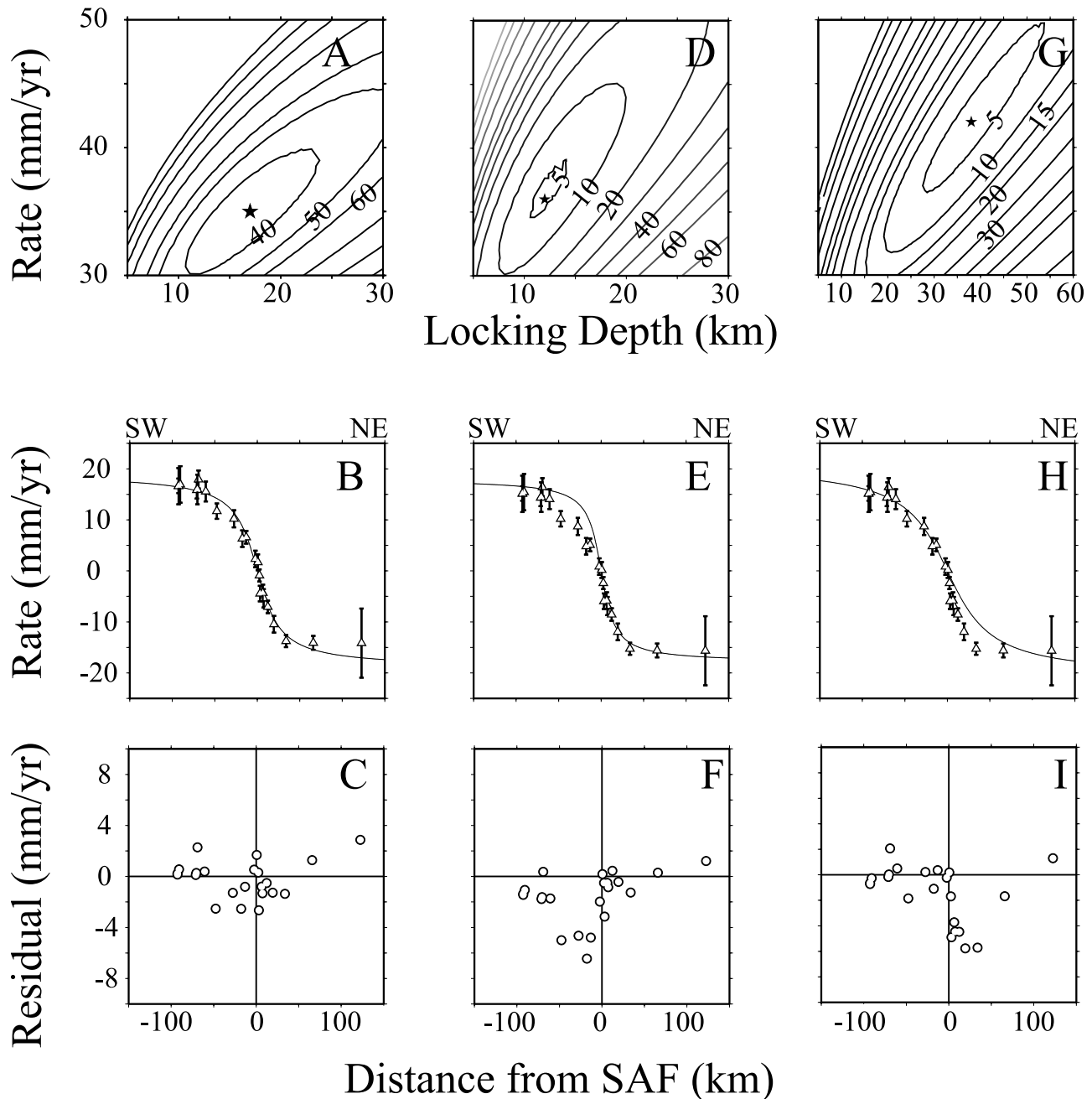


**Figure 5.** GPS velocity data compared to simple elastic half-space models, adjusting fault slip rate and locking depth for best fit, using (a, b, c) all data; (d, e, f) data NE of SAF; and (g, h, i) data SW of SAF. Star indicates best fit model on plots of  $\chi^2$  misfit (Figures 5a, 5d, and 5g).

of misfit more than expected just from the addition of adjustable parameters? We address this by using variations of the simple elastic half-space model combined with the  $F$  test [e.g., *Stein and Gordon, 1984*]. In the elastic half-space model, the fault locking depth parameter is used to describe the transition from locked to slipping behavior at depth, correlating approximately with the nucleation depth of large earthquakes at the base of the brittle, elastic crust. Faults with shallow locking depths have high surface velocity gradients near the faults, while faults with deep locking depths have low-velocity gradients near the fault.

By definition, a fault can only have one locking depth. However, this parameter is similar to the elastic layer thickness in more sophisticated coupling models (see next section). We therefore modify the simple elastic half-space model to allow different “locking depths” on either side of the fault (physically corresponding to different elastic layer thickness) to account for possible asymmetric strain accumulation. Essentially, we estimate the locking depth on each side of the fault for a fixed fault rate and add the solutions, taking advantage of the linear nature of elastic models. The misfit of the complex model is calculated by adding the

**Table 4a.** Parameters for Elastic Half-Space Model<sup>a</sup>

Best Fit	Rate, mm/yr		Locking Depth (km)		$\chi^2$		
	SAF	LAF	SAF	LAF, Fixed	Total (N = 22)	SW (N = 12)	NE (N = 10)
<i>Single Fault (SAF)</i>							
All	37 <sup>+3.5</sup> <sub>-2.5</sub>	N/A	17 <sup>+5</sup> <sub>-3.5</sub>	N/A	34.64	N/A	N/A
SW	42 <sup>+5</sup> <sub>-2</sub>	N/A	38 <sup>+7</sup> <sub>-4</sub>	N/A	N/A	3.68	N/A
NE	36 <sup>+2</sup> <sub>-1</sub>	N/A	12 <sup>+2</sup> <sub>-1</sub>	N/A	N/A	N/A	4.49
SW <sup>b</sup>	39	N/A	33 ± 2	N/A	N/A	3.98	N/A
NE <sup>b</sup>	39	N/A	14 ± 1	N/A	N/A	N/A	4.94
<i>Two Faults (SAF and LAF)<sup>c</sup></i>							
All	32 ± 4	5 <sup>+0.5</sup> <sub>-1</sub>	16 <sup>+4</sup> <sub>-2</sub>	15	12.84	N/A	N/A
SW	36 <sup>+5</sup> <sub>-2.5</sub>	2 ± 1.5	26 <sup>+5.5</sup> <sub>-4.5</sub>	15	N/A	3.69	N/A
NE	36 <sup>+3</sup> <sub>-2</sub>	N/A	12 <sup>+2.5</sup> <sub>-1.5</sub>	N/A	N/A	N/A	4.49

<sup>a</sup>Rate and locking depth are varied unless otherwise stated; N/A is not applicable; SAF and LAF denote San Andreas Fault and Los Alamos Fault, respectively. “All” means all data are used; “SW” means only data southwest of the fault are used; and “NE” means only data northeast of the fault are used.

<sup>b</sup>Rate held fixed at 39 mm/yr, based on average of best fit rate SW (42 mm/yr) and NE (36 mm/yr) of the fault.

<sup>c</sup>LAF is 59 km SW of SAF, modeled with a fixed locking depth of 15 km.

misfits for each side of the fault. For example, in Table 4a, rate is 39 mm/yr,  $\chi^2_{(complex)} = 3.98 + 4.94 = 8.92$ .

[18] The test compares the simplest elastic half-space model, varying the rate and locking depth (two adjustable parameters) with the complex model that solves for the rate and separate “locking depths” (i.e., different elastic layer thickness) on each side of the fault (three adjustable parameters (Table 4a). The improved fit with the three parameter model is statistically significant at better than 99% confidence (Table 4c).

[19] Maps of Holocene faults suggest the presence of additional active faults southwest of the SAF. In our area, the Los Alamos Fault (LAF) is believed to be active and lies ~60 km southwest of the SAF [Jennings and Saucedo, 1994]. We modify the elastic half-space model to account for this fault, fixing its locking depth to 15 km (Table 4a) and comparing results for a simple three parameter model (rate and locking depth of the SAF, and rate of the LAF) to a more complicated model with four adjustable parameters (rate of the SAF, rate of the LAF, and “locking depths”

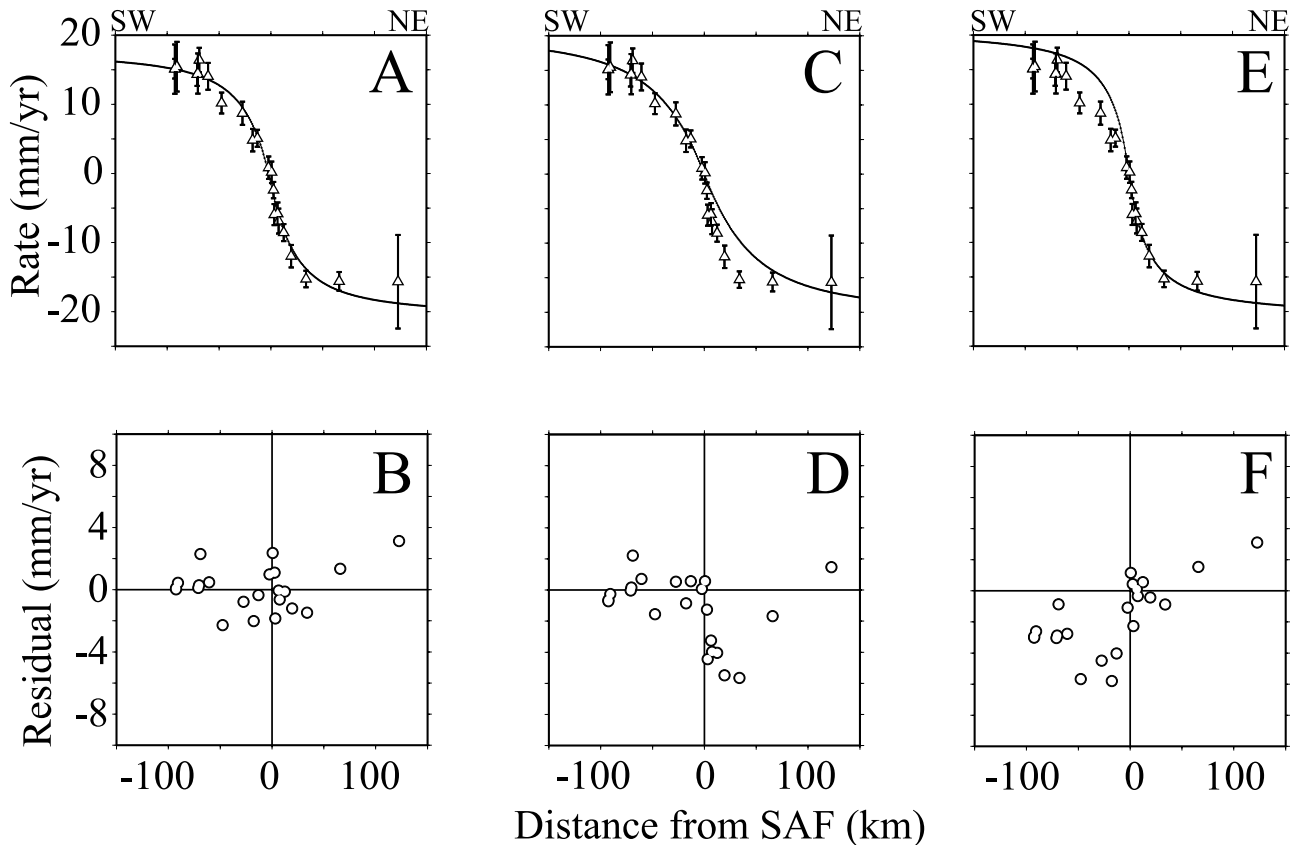


**Figure 6.** GPS velocity data compared to best fit viscoelastic coupling models (Table 4b) for (a) all data; (c) data SW of SAF; (e) data NE of SAF. Data minus model are (b, d, f) corresponding residuals.

**Table 4b.** Parameters for Viscoelastic Coupling Model (Single Fault)<sup>a</sup>

	Rate, mm/yr	Elastic Layer Depth, km	Viscosity, Pa s	Young's Modulus, GPa	$\chi^2$		
					Total (N = 22)	SW (N = 12)	NE (N = 10)
Best fit (all) <sup>b</sup>	39 ± 1	6 ± 1	1.75E19 ± 0.5E19	75	14.37	N/A	N/A
Best fit <sup>c</sup>	35	3 ± 1	1E19	75	47.92	N/A	N/A
Best fit (SW) <sup>d</sup>	42 ± 1	8	3.5E19	200 ± 25	N/A	3.58	N/A
Best fit (NE) <sup>d</sup>	42 <sup>+3</sup> <sub>-2</sub>	8	3.5E19	75 ± 5	N/A	N/A	5.24

<sup>a</sup>Uncertainties for varied parameters calculated from equation (2). Earthquake recurrence interval set at 203 years, and the last earthquake is set at 148 years ago. Read 1.75E19 ± 0.5E19 as  $1.75 \times 10^{19} \pm 0.5 \times 10^{19}$ .

<sup>b</sup>Rate, elastic layer depth, viscosity are varied. Young's modulus fixed at 75 GPa.

<sup>c</sup>Same variables as footnote a, but rate is fixed at 35 mm/yr.

<sup>d</sup>Results for fixed elastic layer depth and viscosity, and variable Young's modulus and rate. Data are fit equally well for models with fixed Young's modulus and elastic layer thickness and variable viscosity and rate.

southwest and northeast of the SAF). Again, the improved fit is significant at better than 99% confidence (Table 4c).

## 4.2. Viscoelastic Coupling Model

[20] Simple coupling models, with an elastic layer coupled to an underlying viscoelastic half-space, have been used for some time to model earth deformation processes [e.g., Nur and Mavko, 1974; Savage and Prescott, 1978; Thatcher, 1983; Segall, 2002]. Savage and Lisowski [1998] describe the surface strain accumulation for an infinitely long vertical strike-slip fault embedded in an elastic layer coupled to an underlying viscoelastic half-space. This model incorporates earthquake cycle effects assuming periodic earthquakes. As with the elastic half-space model, rheologic properties are assumed to be symmetric about the fault. The main parameters in coupling models include the earthquake recurrence interval, the date of the last earthquake, far-field plate rate, elastic layer thickness, an elastic material parameter such as Young's modulus (here assumed equivalent in the elastic and viscoelastic material), and viscosity of the underlying half-space.

[21] This model also fits the data reasonably well (Figures 6a and 6b), though several parameters need to be adjusted to the limits of their uncertainties (Tables 1a, 4b and 4c). Holding the rate fixed at a more reasonable value (35 mm/yr), the fit noticeably worsens (Table 4b). We may also use this model to define asymmetry as we did with the elastic half-space model, obtaining similar estimates of asymmetry: 5 mm/yr 34 km northeast of the fault (Figures 6c and 6d); 6 mm/yr 18 km southwest of the fault (Figures 6e and 6f) (Table 4b). In this case, we can estimate either the thickness of the elastic layer or material properties such as Young's modulus (there are tradeoffs among some parameters). Improved fits are obtained when the elastic layer is thinner on the northeast side of the fault, or with a uniform layer thickness across the fault if Young's modulus northeast of the fault is less than the value southwest of the fault.

[22] In summary, surface strain accumulation across the Carrizo segment of the San Andreas Fault is asymmetric, with a region of high-velocity gradient northeast of the fault. This suggests the presence of a weak zone northeast of the fault. For both elastic half-space and viscoelastic coupling models, improved fits are obtained by either thinning the elastic layer and/or weakening the material northeast of the fault. The asymmetry reaches a maximum of 5–6 mm/yr, and is most evident relatively close to the fault (<35 km) suggesting some constraint on source

depth. The spatial scale of the anomaly is of the order of the crustal thickness, suggesting a source in the crust rather than the upper mantle. We next examine a series of strain accumulation models incorporating laterally varying mechanical properties in the crust, implemented numerically via a finite element approach, and compare best fit parameter values to independent data.

## 5. Asymmetric Strain Accumulation Models

### 5.1. Finite Element Model

[23] Finite element models can be used to simulate complex spatial variations in fault geometry and material properties. Here we focus on simple coupling models with an elastic layer welded (coupled) to underlying viscoelastic material in a two-dimensional cross section normal to the fault. The models are “true plane strain”, i.e., we allow displacements but not displacement gradients in the out of plane direction (the model is referred to as ‘2.5D’ since motion occurs normal to the plane of the cross section). The out of plane direction is parallel to the strike of the fault. The model thus takes advantage of the relatively simple geometry of the Carrizo segment of the SAF and the observation that site velocities are essentially parallel to fault strike for both North America and Sierra Nevada block reference frames (e.g., Figure 1).

[24] Our finite element method solves the mechanical equilibrium equation for three-dimensional displacements in directions  $x$  and  $y$  parallel to the studied cross section and  $z$  perpendicular to it. Displacement gradients in the  $z$  direction are assumed to vanish, i.e., displacements (velocities) are presumed identical in parallel cross sections. We developed the code from G-TECTON version 1.3 [1989] [Melosh and Raefsky, 1980; Govers, 1993]. Constitutive

**Table 4c.**  $F$  Test (N = 22)

	$\chi^2$	$r^a$	$p^b$	Confidence Level, %
<i>One-Fault Elastic Half-Space Model</i>				
Simple	34.64	2	N/A	
Complex	8.92	N/A	3	
<i>Two-Fault Elastic Half-Space Model</i>				
Simple	12.84	3	N/A	>99
Complex	8.18	N/A	4	>99

<sup>a</sup>The parameter  $r$  is the number of adjustable parameters for a simple model.

<sup>b</sup>The parameter  $p$  is the number of adjustable parameters for a complex model.

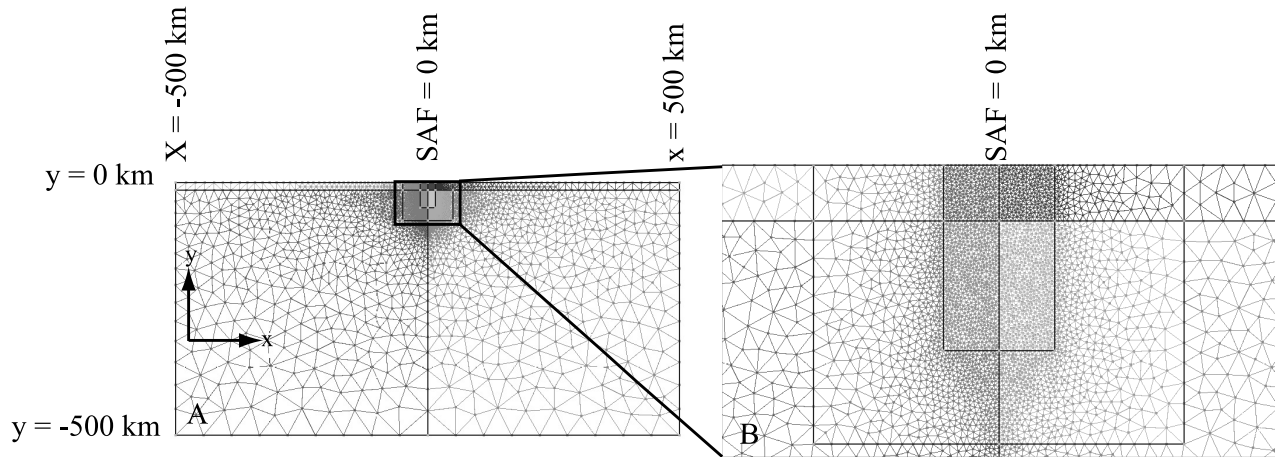


**Figure 7.** Schematic of a sample mesh for our finite element models. (a) Entire mesh, and (b) area near the fault. Mesh extends 500 km on either side of SAF and down 500 km to reduce edge effects. The SAF (located in the elastic layer at  $x = 0$  km) is defined by the split node method of *Melosh and Raefsky* [1981]. The fault extends to the base of the elastic layer. Node density is increased near the fault to reduce mesh-related effects.

equations are based on (compressible) elastic and nonlinear, incompressible viscous flow:

$$\dot{\epsilon}_{xx} = \frac{(1 + \nu)}{E} [(1 - \nu)\dot{\sigma}_{xx} - \nu\dot{\sigma}_{yy}] + \frac{(\sigma_E/\eta_{\text{eff}})^{n-1}}{4\eta_{\text{eff}}} [\sigma_{xx} - \sigma_{yy}] \quad (3a)$$

$$\dot{\epsilon}_{yy} = \frac{(1 + \nu)}{E} [(1 - \nu)\dot{\sigma}_{yy} - \nu\dot{\sigma}_{xx}] - \frac{(\sigma_E/\eta_{\text{eff}})^{n-1}}{4\eta_{\text{eff}}} [\sigma_{xx} - \sigma_{yy}] \quad (3b)$$

$$\dot{\epsilon}_{xy} = \frac{1 + \nu}{E} \dot{\sigma}_{xy} + \frac{(\sigma_E/\eta_{\text{eff}})^{n-1}}{2\eta_{\text{eff}}} \sigma_{xy} \quad (3c)$$

$$\dot{\epsilon}_{xz} = \frac{1 + \nu}{E} \dot{\sigma}_{xz} + \frac{(\sigma_E/\eta_{\text{eff}})^{n-1}}{2\eta_{\text{eff}}} \sigma_{xz} \quad (3d)$$

$$\dot{\epsilon}_{yz} = \frac{1 + \nu}{E} \dot{\sigma}_{yz} + \frac{(\sigma_E/\eta_{\text{eff}})^{n-1}}{2\eta_{\text{eff}}} \sigma_{yz} \quad (3e)$$

where  $\dot{\epsilon}_{ij}$  are components of the strain rate tensor, a dot indicates differentiation with respect to time,  $E$  is Young's modulus,  $\nu$  is Poisson's ratio,  $\sigma_{ij}$  are components of the Cauchy stress tensor,  $\eta_{\text{eff}}$  is the effective viscosity, and  $\sigma_E$  is the effective stress, defined as

$$\sigma_E \equiv \sqrt{\left(\frac{\sigma_{xx} - \sigma_{yy}}{2}\right)^2 + \sigma_{xy}^2 + \sigma_{xz}^2 + \sigma_{yz}^2} \quad (4)$$

Equation (4) avoids problems related to maintaining incompressibility. We account for geometric nonlinearity due to large deformation through the formalism of *McMeeking and Rice* [1975]. Simplex elements are used

to derive the finite element equations. Matrix equations are solved using PETSc (<http://www.mcs.anl.gov/petsc>) [*Balay et al.*, 2002], a suite of data structures and routines for the scalable solution of partial differential equations. We adopt the conjugate gradient implementation of the Krylov subspace method and Eisenstat preconditioning to solve the algebraic equations iteratively. The model has been tested extensively, including comparisons to analytical results, some of which are presented for the first time in this paper.

[25] All finite element models presented here extend horizontally 500 km on either side of the fault, and vertically  $-500$  km from the surface (encompassing both elastic and viscoelastic layers) to reduce edge effects, and to simulate the half-space of the analytic solution. To reduce errors due to the mesh itself, we increase the number of nodes (and therefore elements) around the fault (Figures 7a and 7b). A known displacement is applied at every earthquake cycle on the locked fault via the split node method [*Melosh and Raefsky*, 1981]. The fault extends from the surface to the base of the elastic layer. The elastic properties of our model are defined by Poisson's ratio and Young's modulus. We fix Poisson's ratio at a value of 0.25, and for some models vary Young's modulus. For some models we fix the slip rate of the fault to its known Holocene average. For all models we fix earthquake recurrence interval (205 years) based on the best estimates of these parameters from geologic data (Tables 1a and 5). The date of the last earthquake (1857) is well known based on historical data (Tables 1a and 5). Model results are therefore displayed at 150 years after the last earthquake.

[26] We focus on two possible sources of asymmetry: case I, contrast in elastic layer thickness across the fault, with otherwise uniform material properties (Figures 8a and 8b), and case II, uniform elastic layer thickness, with a contrast in material properties across the fault (Figures 8c and 8d). In case I, the viscosity of the underlying material and the elastic layer thickness on the northeastern side of the fault are varied. For most models, the thickness on the

**Table 5.** Parameters for Finite Element Models<sup>a</sup>

Case	Rate, mm/yr		Viscosity, Pa s	Elastic Layer Thickness, km		Young's Modulus, GPa			Width of Weak Zone, km	$\chi^2$	$\chi_r^{2b}$
	SAF	LAF		SW of SAF	NE of SAF	SW of SAF	Weak Zone	NE of Weak Zone			
I <sup>c</sup>	34	0	4E19 <sup>d</sup>	10 <sup>d</sup>	8 <sup>d</sup>	75	75	75	N/A	20.06	1.08
II <sup>e</sup>	36	0	3E19 <sup>d</sup>	15	15	50 <sup>d</sup>	30 <sup>d</sup>	75	15 <sup>d</sup>	14.77	0.82
III <sup>f</sup>	38 <sup>+1.5</sup> <sub>-2</sub>	0	3E19 <sup>+1.5E19</sup> <sub>-0.5E19</sub>	15	15	50 <sup>d</sup>	40 ± 5	75	15 <sup>d</sup>	12.51	0.74
IVA <sup>g</sup>	34	3 <sup>d,f</sup>	3E19 <sup>d</sup>	10 <sup>d</sup>	8 <sup>d</sup>	75	75	75	N/A	10.83	0.60
IVB <sup>h</sup>	36 <sup>+2</sup> <sub>-1.5</sub>	3 ± 1	3E19 <sup>+1.5E19</sup> <sub>-0.5E19</sub>	15	15	50 <sup>d</sup>	40 ± 8	75	25 <sup>d</sup>	9.30	0.58

<sup>a</sup>For all models, earthquake recurrence interval set to 205 years and the last earthquake set to 150 years ago. Estimated parameters are listed with plus/minus one standard deviation, as determined by equation (2), except as noted in footnote d. N/A denotes not applicable. SAF and LAF represent San Andreas Fault and Los Alamos Fault, respectively.

<sup>b</sup>Reduced  $\chi^2$ , defined as  $\chi^2/N-p$ , where  $N$  is the number of data (22) and  $p$  is the number of adjusted parameter.

<sup>c</sup>Laterally uniform material properties, different elastic layer thickness on each side of fault, fixed SAF rate. Three adjusted parameters (Figures 13 and 14a).

<sup>d</sup>Estimated parameter, minimum misfit value reported. Significant trade off with other estimated parameters precludes meaningful uncertainty estimate.

For the width of the weak zone, a minimum estimate is defined (~5 km smaller than listed value) but not a maximum estimate.

<sup>e</sup>Laterally uniform elastic layer thickness, different material properties on each side of fault, fixed SAF rate. Four adjusted parameters (Figures 14b and 16).

<sup>f</sup>Similar to case II, with variable SAF rate. Five adjusted parameters (Figure 17).

<sup>g</sup>Similar to case I, with variable LAF rate. Four adjusted parameters (Figure 19a).

<sup>h</sup>Similar to cases II and III, with variable SAF and LAF rate. Six adjusted parameters (Figures 18 and 19b). For cases IVA and IVB, LAF is modeled with an elastic half-space dislocation, with locking depth fixed at 10 km (case IVA) or 15 km (case IVB), and located 59 km SW of SAF.

southwest side is fixed to 10 km, and only the thickness on the northeast side is varied. Some models were also run with an elastic layer thickness of 15 km southwest of the fault, but this did not change results significantly. The fault slip rate is fixed at 34 mm/yr. Young's modulus is fixed (75 GPa) and is identical on each side of the fault (Table 5). Thus a total of three parameters may be considered variable in this model (viscosity, and elastic layer thickness on each side of the fault).

[27] In case II, we hold the elastic layer thickness fixed, and vary four other parameters: the viscosity of the under-

lying material, the width and Young's modulus of a weak zone within the elastic layer northeast of the fault, and Young's modulus of the elastic layer southwest of the fault (for most models this is fixed to 50 GPa). The fault slip rate is held at 36 mm/yr. Young's modulus of the elastic layer northeast of the weak zone is also fixed at 75 GPa (Table 5).

[28] Case III models are similar to those in case II, differing only because the SAF rate is also varied, for a total of five adjustable parameters. We investigated rates between 25 and 50 mm/yr (Table 5).

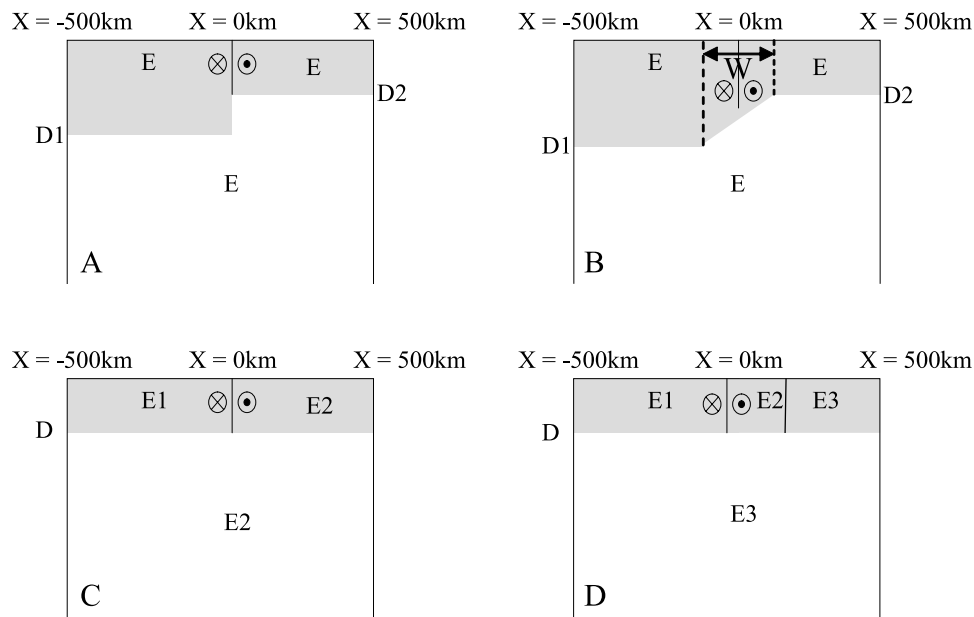


**Figure 8.** Schematic illustration of some of the models implemented for this study with finite element technique. (a) Uniform elastic properties, variable elastic layer thickness, (b) finite depth transition zone (see text), and (c, d) uniform elastic layer thickness, variable Young's modulus. Note narrow region of soft material (E2) adjacent to fault in Figure 8d. Case I and II models (Table 5) are illustrated by Figures 8b and 8d, respectively.

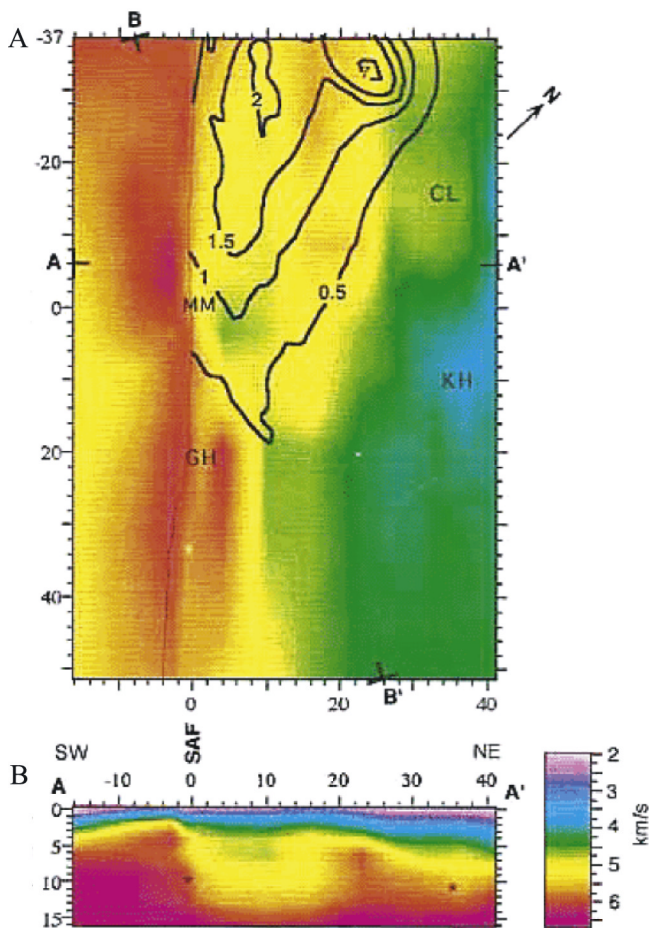


**Figure 9.**  $P$  wave seismic velocity of the Parkfield region [Eberhart-Phillips and Michael, 1993]. (a) Plan view of solution at 4 km depth and (b) southwest-northeast (A-A') cross sections.  $P$  wave velocity color scale is in lower right. Note region of low  $P$  wave velocity northeast of fault, approximately 20 km wide, to a depth of  $\sim 15$  km.

[29] Case IVA and IVB models additionally include the effect of the Los Alamos Fault (LAF) located 59 km southwest of the SAF, modeled as a simple elastic half-space dislocation with 15 km locking depth. Case IVA is similar to case I, but with a total of four adjustable parameters, and case IVB is similar to cases II and III, but with a total of six adjustable parameters.

[30] Other parameters are fixed to values listed in Table 5. Below we review available constraints on key model parameters.

### 5.2. Elastic Layer Thickness

[31] Large earthquakes tend to nucleate near the base of the elastic layer, near the brittle-ductile transition zone. Below this depth, significant elastic strain does not accumulate and earthquakes do not occur. The seismogenic depth interval is usually equated with the portion of the lithosphere that has substantial strength [Sibson, 1983]. For our simple models, we relate the observed seismogenic depth interval to the elastic layer thickness. Seismic data in our study area are very sparse (Figure 2 and 3), reflecting the fact that this segment is currently locked and has not

experienced a major earthquake since 1857. Most events occur above 20 km, although the majority of events on the southwest side take place above 10 km (Figure 3). Case I and IVa models have variable elastic thickness northeast of the SAF (5–25 km), while the southwest side is fixed at 10 km.

### 5.3. Width of the Elastic Layer Transition Zone

[32] For vertical strike-slip faults with contrasting elastic layer thicknesses on each side of the fault, the geometry of the transition between the two sides of the fault could affect the pattern of surface strain accumulation. The transition may be an abrupt step or gradual. We assume a simple sloping transition and assume that the fault occupies the center of the sloping zone (Figure 8b). In a series of preliminary model experiments we tested transition widths between 0 and 30 km. This parameter turned out to have little effect on the pattern of surface strain accumulation. For case I and IVA models discussed below, we fixed the transition width to 1 km.

### 5.4. Elastic Properties

[33] The elastic properties of the material surrounding a fault can affect the pattern of strain accumulation. The elastic moduli of typical crustal rocks are determined experimentally. They may also be estimated from seismic wave velocity. For example, assuming a Poisson's ratio of 0.25,

$$v_p = ((6/5)E/\rho)^{1/2} \quad (5)$$

where  $v_p$  is the  $P$  wave velocity,  $\rho$  is density, and  $E$  is Young's modulus [Stein and Wysession, 2003]. A typical crustal value for Young's modulus is  $\sim 75$  GPa [Stein and Wysession, 2003], but variations within a factor of 2 of this value can occur in the upper crust. Eberhart-Phillips and Michael [1993] mapped the three-dimensional seismic velocity structure across the San Andreas Fault in the Parkfield region of central California, immediately north of our study area. They found low seismic velocities in the upper crust for a 20 km wide region northeast of the fault compared to equivalent depths southwest of the fault (Figure 9). This suggests lower values of Young's modulus and/or higher density northeast of the fault (Figure 9b). Assuming equivalent density on each side of the fault at a given depth implies that rocks northeast of the fault have a lower Young's modulus, i.e., are weaker. At a depth of 10 km, assuming a density of  $2700 \text{ kg/m}^3$ , rocks on the northeast side of the fault have a Young's modulus that is about 40% lower than rocks southwest of the fault. Our strain accumulation data (with higher velocity gradients northeast of the fault implying weaker material) suggest a similar pattern in the Carrizo segment. The SCEC seismic velocity model version 3.0 (<http://www.data.scec.org/3Dvelocity/3Dvelocity.html>) suggests a similar anomaly, although data in our study area are quite sparse.

[34] For models with uniform elastic layer thickness (cases II, III, and IVB) we define a narrow (5–25 km wide) weak zone east of the fault, with variable Young's modulus. Crust southwest of the fault also has variable Young's modulus. Northeast of the weak zone, the Young's modulus of the crust is set to 75 GPa (Figure 8d). Young's modulus

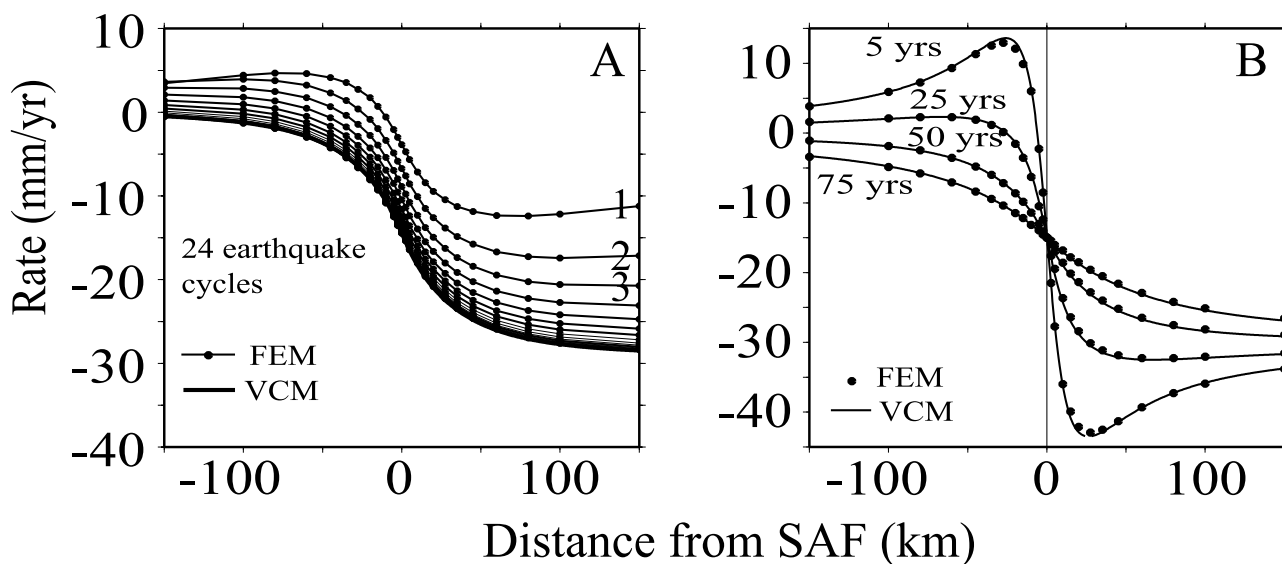


**Figure 10.** (a) Convergence of the finite element model (FEM) after several iterations (lines with dots; first 3 iterations labeled), compared to the equivalent analytic viscoelastic coupling model (VCM; heavy solid line). (b) Comparison of converged FEM results (dots) at various times after an earthquake to corresponding analytic VCM (solid line).

of the viscoelastic layer is set equal to the highest value for Young’s modulus in the elastic layer (75 GPa). We searched a factor of three higher or lower than the nominal value in model areas with variable Young’s modulus to define low-misfit solutions.

**5.5. Half-Space Viscosity**

[35] The viscosity of the material below the elastic layer (half-space in the analytical coupling model) has a strong influence on the pattern of surface strain accumulation. For a simple model of an elastic layer over a viscoelastic half-space (similar to our mechanical model) *Kenner and*

*Segall* [2000, 2003] estimate half-space viscosity in the San Francisco region of  $\sim 3 \times 10^{19}$  Pa s based on geodetically determined postseismic response to the 1906 earthquake. We tested values of viscosity in the range  $1 - 6 \times 10^{19}$  Pa s.

**5.6. Validation of FEM**

[36] To validate our finite element model, we set up a simple symmetric case for comparison to the analytic coupling model of *Savage and Lisowski* [1998]. All parameters in the two models were set to the same (or equivalent) values. The modeled fault is locked during the

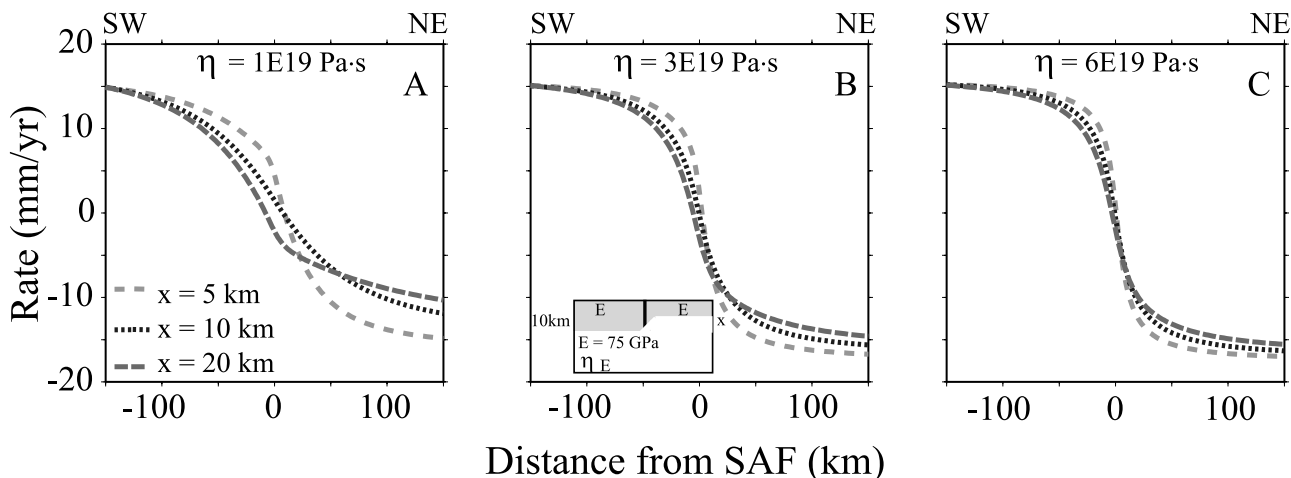


**Figure 11.** Predictions of finite element model for case I models; variable elastic layer thickness northeast of fault ( $x$ ), for  $\eta =$  (a)  $10^{19}$ , (b)  $3 \times 10^{19}$ , and (c)  $6 \times 10^{19}$  Pa s (Table 5). Southwest side of the SAF is fixed to 10 km. Asymmetric behavior is more noticeable when viscosity is low (Figure 11a). Velocity predictions are “pinned” (made equal) 150 km southwest of fault, to better illustrate model differences near the fault.

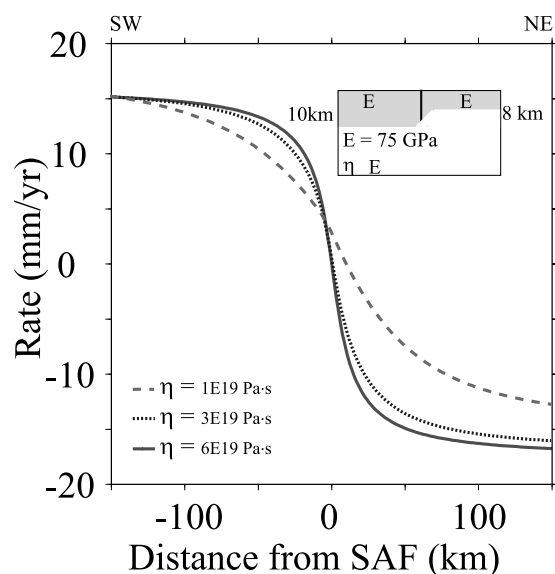


**Figure 12.** Effect of variable viscosity on predicted surface velocity assuming a contrast of elastic layer thickness of 2 km for case I models (Table 5, our best fitting result). Velocity predictions are “pinned” (made equal) 150 km southwest of fault, to better illustrate model differences near the fault.

interseismic period in the elastic upper crust, while viscous deformation occurs in the layer beneath. Horizontal movements are controlled by the earthquake cycle, governed by the recurrence time of earthquakes. The fault is unclamped in the finite element model to simulate an earthquake, and slips by an amount such that the seismic slip divided by the recurrence time gives the long-term slip rate (34 mm/yr, cases I, and IVA; 36 mm/yr, case II; variable slip rates for cases III, and IVB; Table 5). Both models are strictly periodic, and assume steady state conditions have been reached, i.e., an infinite number of earthquake cycles have occurred. Depending on half-space viscosity, the FEM converges to steady state (and agreement with the analytical coupling model) after about 20 earthquake cycles (Figure 10a). Models with lower values of viscosity converge faster. Extraneous behavior due to sizing of the mesh elements is not observed, indicating that the mesh size we use in this study is appropriate for the problem (Figures 7, 10a, and 10b).

## 6. Model Results

### 6.1. Case I: Variation of Elastic Layer Thickness

[37] Table 5 and Figures 11, 12, 13, and 14a show results for variable elastic thickness models, for a limited range of viscosities ( $1\text{--}6 \times 10^{19}$  Pa s). Case I results agree in a qualitative way with our previously described analytic models: a thinner elastic layer northeast of the fault is required to fit the geodetic data. The best fit to the GPS data is obtained with an elastic layer thickness of 8 km northeast of the fault, shallower than the 10 km elastic layer thickness southwest of the fault (Figure 14a and Table 5). Models with viscosities between  $3$  and  $5 \times 10^{19}$  Pa s and elastic layer thicknesses of  $\sim 7\text{--}9$  km east of the fault fit the geodetic data quite well. As the elastic

layer thickness northeast of the fault increases, higher viscosities are required to fit the data (Figure 13 and Table 5), illustrating known parameter trade-offs observed in homogenous viscoelastic coupling models.

### 6.2. Case II: Variation of Elastic Properties

[38] Table 5 and Figures 14b, 15, and 16, show results for models with uniform elastic layer thickness and variable width and Young’s modulus of a weak zone northeast of the fault, for the same viscosity range as case I. While the data define an optimum width of the weak zone ( $\sim 15$  km) and its minimum extent ( $\sim 10$  km) (Figures 16a and 16b), the exact value depends on the ratio of viscosity to Young’s modulus, and the maximum width is undefined. Estimates of viscosity and Young’s modulus of the weak zone correlate to some extent (Figure 16c).

### 6.3. Case III: Variation of San Andreas Fault Slip Rate

[39] In the models discussed so far, we have fixed the key geologic parameters (fault slip rate, recurrence interval, and date of last earthquake) to their known values based on geological or historic information, and adjusted rheological parameters to obtain a best fit solution. It is also useful to ask whether a mechanical model based on our preferred rheology would allow us to estimate the geological parameters, i.e., assuming that they were not known. Here we explore this problem in a limited way, varying the fault slip rate and two key rheological parameters (effective viscosity, Young’s modulus of the weak zone), and keeping other parameters fixed to their previous best fit values. Elastic layer thickness is fixed to 15 km. Results are displayed in Figures 17a and 17b. Ignoring the Los Alamos Fault, the best fit rate is  $38 \pm 2$  mm/yr, marginally faster than Holocene rate,  $34 \pm 3$  mm/yr, although equivalent within uncertainties, and similar to other recent geodetic estimates,

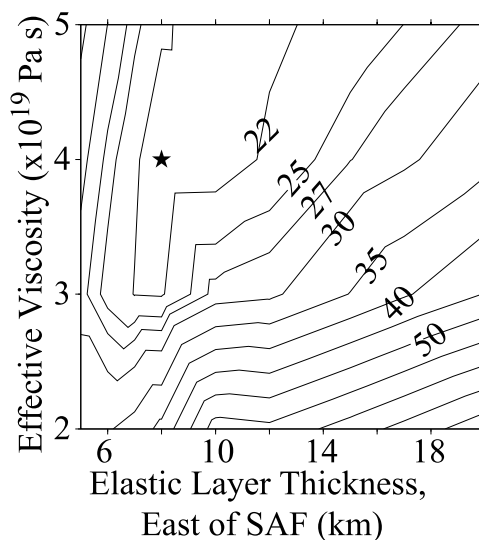


**Figure 13.** The  $\chi^2$  misfit for case I models with variable viscosity and elastic layer thickness northeast of SAF, assuming laterally uniform elastic properties. In this example,  $\chi^2 = \sim 27$  represents approximate 95% confidence limit. Viscosities less than about  $2.5 \times 10^{19}$  Pa s are precluded by the data, but an upper bound value is not defined (Table 5).

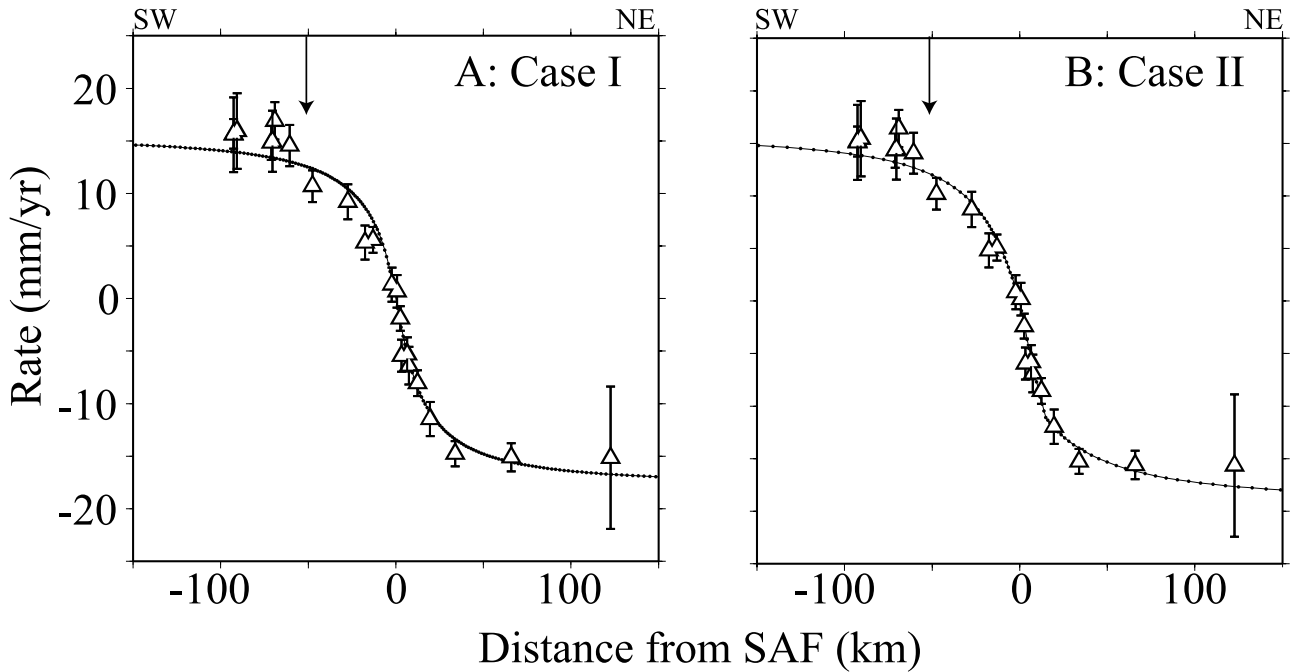


**Figure 14.** GPS data compared to best fit model for (a) case I (variable elastic layer thickness), and (b) case II (variable elastic properties). Arrow marks location of the Los Alamos Fault, with known Holocene activity, unaccounted for in these models. Case II is consistent with seismic data suggesting a low-velocity (weak?) zone northeast of SAF.

e.g., 36 mm/yr based on an elastic half-space block model [Meade and Hager, 2005].

**6.4. Case IV: Los Alamos Fault**

[40] The slightly faster SAF rate estimated in case III models may be influenced by several mm/yr of motion on the Los Alamos Fault (LAF), southwest of the Carrizo segment (Figure 2) [Jennings and Saucedo, 1994], and/or strain accumulation on the San Gregorio-Hosgri Fault or other offshore faults, unaccounted for in our simplest finite element models (cases I, II, and III).

Case IVA and IVB models account for motion on the LAF, 59 km southwest of the SAF, using a simple elastic half-space approximation and a locking depth of 10 km (case IVA) and 15 km (case IVB). Case IVA is similar to case I (variable elastic layer thickness, fixed Young’s modulus and SAF rate), while case IVB is similar to cases II and III (uniform elastic layer thickness, variable Young’s modulus and width of the weak zone, variable SAF rate). Incorporating the LAF into the models significantly reduces misfit for both cases IVA and IVB and reduces the best fit SAF rate in case IVB

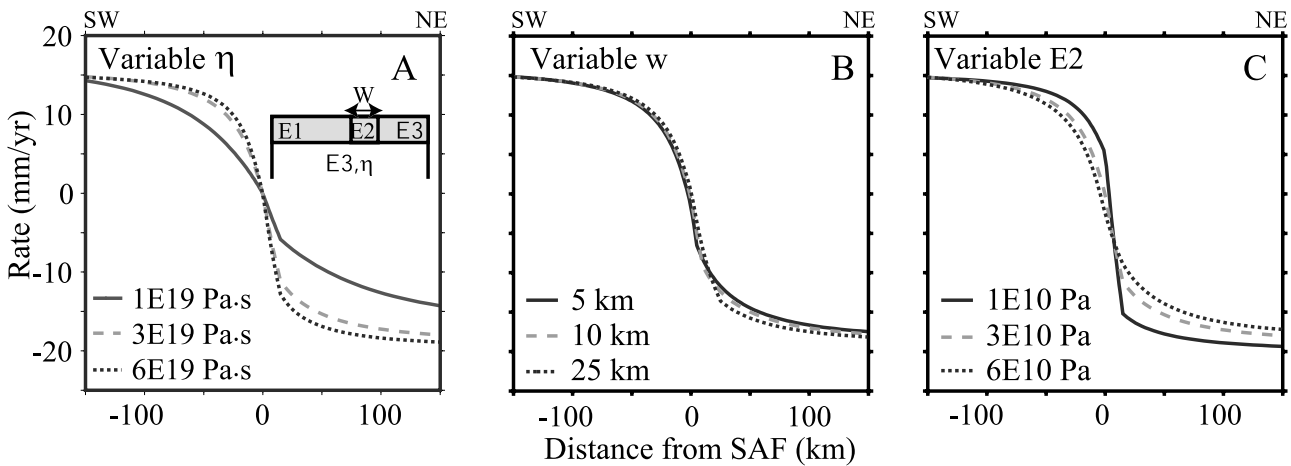


**Figure 15.** Predictions of case II models (uniform elastic layer thickness, variable width, and Young’s modulus of a weak zone northeast of the fault) for (a) variable viscosity, (b) variable width of the weak zone, and (c) variable Young’s modulus of the weak zone (Table 5). Velocity predictions are “pinned” (made equal) 150 km southwest of fault to better illustrate model differences near the fault.

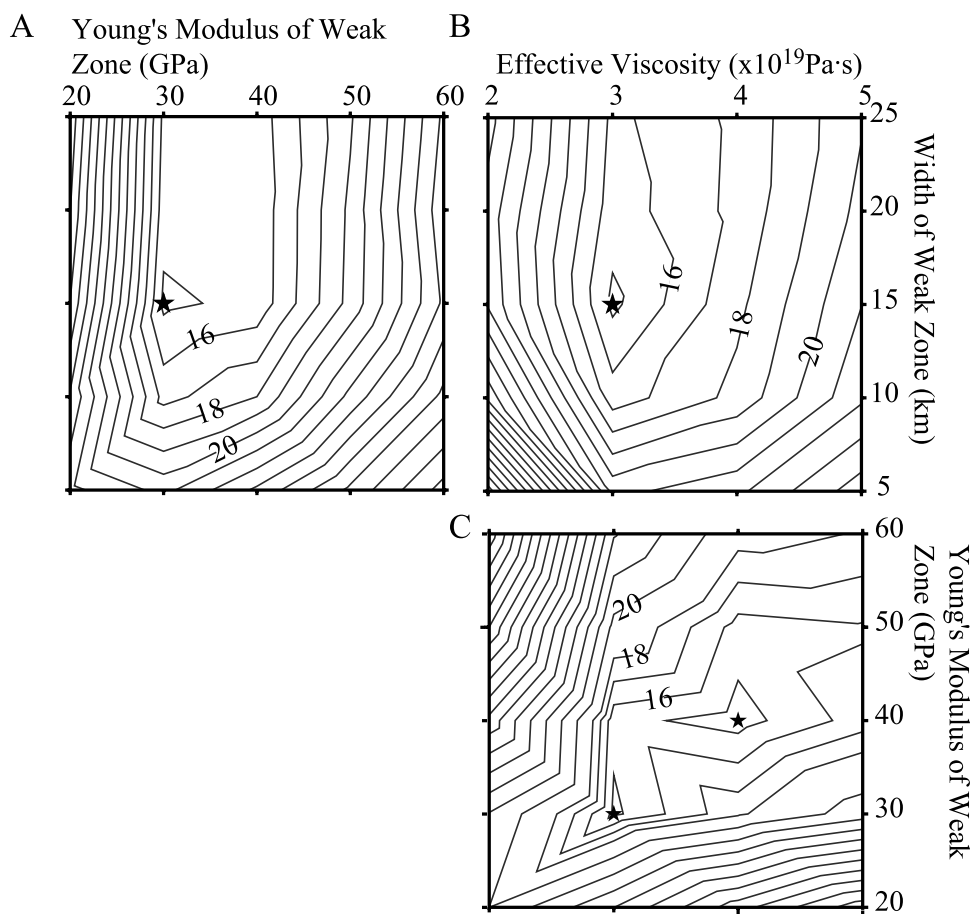


**Figure 16.** Contours of  $\chi^2$  misfit for case II models (uniform elastic layer thickness, variable width and Young's modulus of a weak zone northeast of the fault). A  $\chi^2$  of  $\sim 24$  represents approximate 95% confidence level. Stars mark best fitting results. Note that a minimum width of the weak zone is defined, but not a maximum width (Figures 16a and 16b). Note apparent double minimum in Figure 16c ( $\chi^2 \sim 14.5$ ), reflecting coarseness of grid search and correlation between viscosity and Young's modulus. Independent data for viscosity or Young's modulus are needed to adequately constrain this model.

( $36_{-1.5}^{+2}$  mm/yr; Figures 18 and 19b), but has negligible impact on other parameter estimates (Table 5).

[41] We conclude that models with laterally varying mechanical properties match the geodetic data for the Carrizo segment of the SAF, are consistent with Holocene slip rate data, and are consistent with seismically determined mechanical properties of the upper crust in the region.

## 7. Discussion and Conclusions

[42] New geodetic data on the Carrizo segment of the San Andreas Fault in central California show a clear pattern of asymmetric strain accumulation, confirming earlier suggestions of asymmetry based on EDM observations [Lisowski *et al.*, 1991]. Higher velocity gradients occur northeast of the fault compared to southwest of the fault. If the geodetic data on one side of the fault are fit with a symmetric model, systematic misfits occur on the other side, reaching a maximum of  $\sim 6$  mm/yr within about 20 km from the fault, the approximate crustal thickness in this area. This suggests that the source of the asymmetry lies in the crust.

[43] We tested a variety of strain accumulation models to investigate the source of asymmetric strain accumulation. Our results suggest that the explanation for asymmetric strain accumulation here lies in the laterally variable elastic properties of the upper crust. Most of our models involve an elastic upper layer coupled to underlying viscoelastic material, with mechanical properties loosely corresponding to the upper crust and lower crust/upper mantle respectively. Models with laterally uniform material properties but variable elastic layer thickness (thinner crust northeast of the fault), and models with uniform layer thickness but laterally variable mechanical properties (smaller Young's modulus northeast of the fault) fit the geodetic data equally well. However, consideration of other data strongly supports the latter model. Specifically, models with a uniform elastic layer thickness (15 km) with a 15–20 km wide weak zone (Young's modulus roughly 20–50% weaker than typical crustal material) northeast of the fault fit the geodetic data quite well (Figure 14b), and are also consistent with a variety of seismic and magnetotelluric data, as described in the following paragraphs. It is also consistent with geologic observations and corresponding laboratory data for the major rock types in the region. Granites and

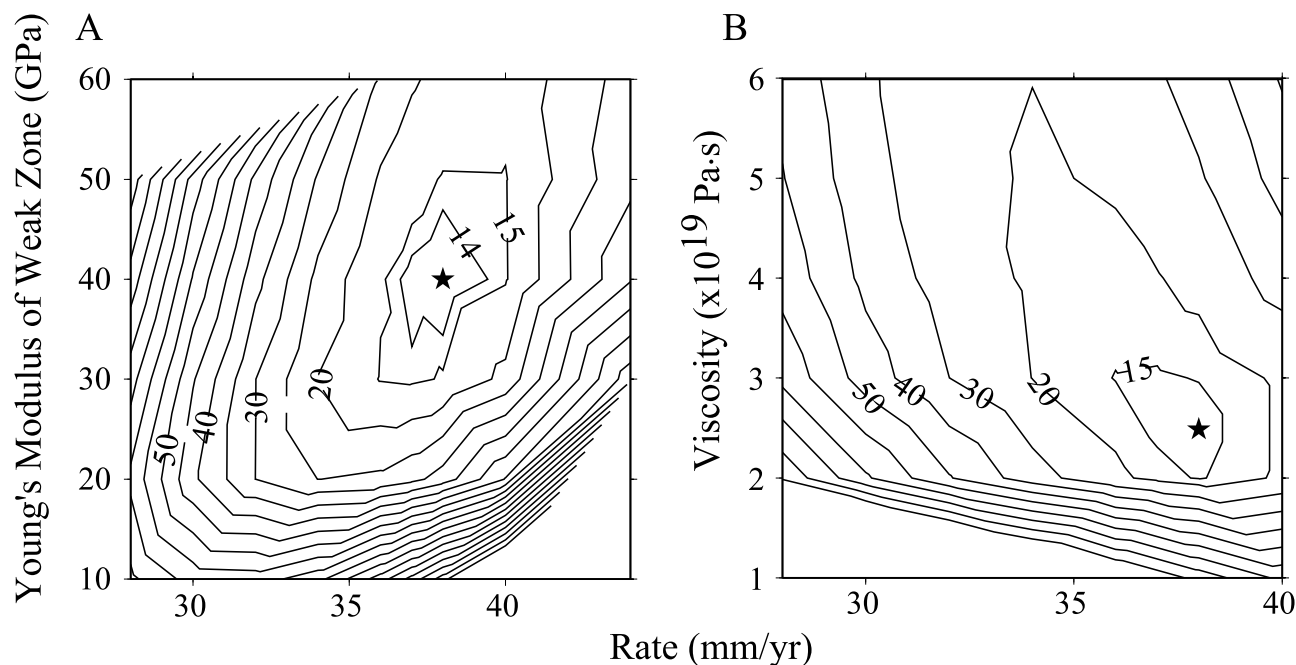


**Figure 17.** Contours of  $\chi^2$  misfit for case III models with variable SAF rate, viscosity, and Young's modulus of the weak zone. Other parameters held to their best fit value for case II (Table 5). Star marks best fit values.  $\chi^2 \sim 22$  represents approximate 95% confidence level.

granodiorites of the Salinian block tend to be stronger (higher Young's modulus) than sedimentary rocks of the Franciscan terrane [e.g., *Turcotte and Schubert*, 2002], and are also presumably stronger than Franciscan mélanges consisting of sedimentary and metamorphic rocks.

[44] Because this segment of the San Andreas Fault is currently locked and accumulating strain, large earthquakes have not occurred here since the deployment of seismometers in California, in contrast to the creeping Parkfield segment to the northwest (Figure 2). The depth distribution of available regional seismicity (<http://neic.usgs.gov>) (Figure 3) suggests that the depth to base of the seismogenic zone (maximum depth of earthquakes, roughly equivalent to the depth of the elastic layer in our strain accumulation models) may actually be deeper northeast of the fault compared to southwest of the fault. This contrasts with the geodetic model results, which require thinner elastic crust northeast of the fault for models with laterally uniform rheologic properties. This mismatch may reflect the small number of seismic events in the Carrizo segment. Estimation of elastic layer thickness from the sparse earthquake data subsets on either side of the fault here may not be statistically meaningful. Another explanation may be that most earthquakes in the current catalog occurred more than 20 km from the fault (Figures 2 and 3) and hence may not be representative of conditions in or near the fault zone.

[45] The seismic velocity data of *Eberhart-Phillips and Michael* [1993] for the Parkfield segment, immediately north of our study area, show a  $\sim 20$  km wide upper crustal ( $<10$  km depth) low-velocity section northeast of the fault (Figure 9). The seismic velocity data are consistent with values of Young's modulus that are about 40% smaller than typical crustal values assuming similar densities. This is similar, both in spatial dimensions of the weak zone

( $>10$  km wide in our result; 20 km in the seismic result) and magnitude of Young's modulus, to our estimates for the Carrizo segment to the south.

[46] Magnetotelluric data suggest similar results. *Unsworth and Bedrosian* [2004] show a zone of low resistivity in the same region as *Eberhart-Phillips and Michael* [1993] find low  $P$  wave velocities. This could reflect a region of excess fluid in Franciscan assemblages or Great Valley sedimentary rocks, contributing to mechanically weaker behavior compared to Salinian block igneous rocks.

[47] Of course, along-strike variations in mechanical properties may occur, and the Parkfield seismic results do not necessarily apply to our study area to the south. However, *Shapiro et al.* [2005] use background seismic noise to delineate crustal asymmetries in surface wave velocities throughout a larger region, including our study area. Their results support lateral variation of seismic velocity (and by inference, elastic properties) across the San Andreas Fault in the upper 20 km of crust for both the Parkfield and Carrizo segments. Their findings also show that the anomalies are restricted to the upper crust; deeper regions are relatively homogenous, justifying our model of a homogeneous viscoelastic region beneath a laterally heterogeneous elastic layer. Our models show that lateral variations in mechanical properties have the most affect on strain accumulation patterns when the variation occurs close to the fault, within  $\sim 10$ – $20$  km, depending on viscosity and Young's modulus. In fact, models whose weak zone extends throughout the entire northeast side of the model space fit the data nearly as well as our best fit model, with a relatively narrow weak zone (Figures 16a and 16b). In effect, all strain required to achieve the "far-field" fault rate has been accommodated within  $\sim 10$ – $20$  km from the

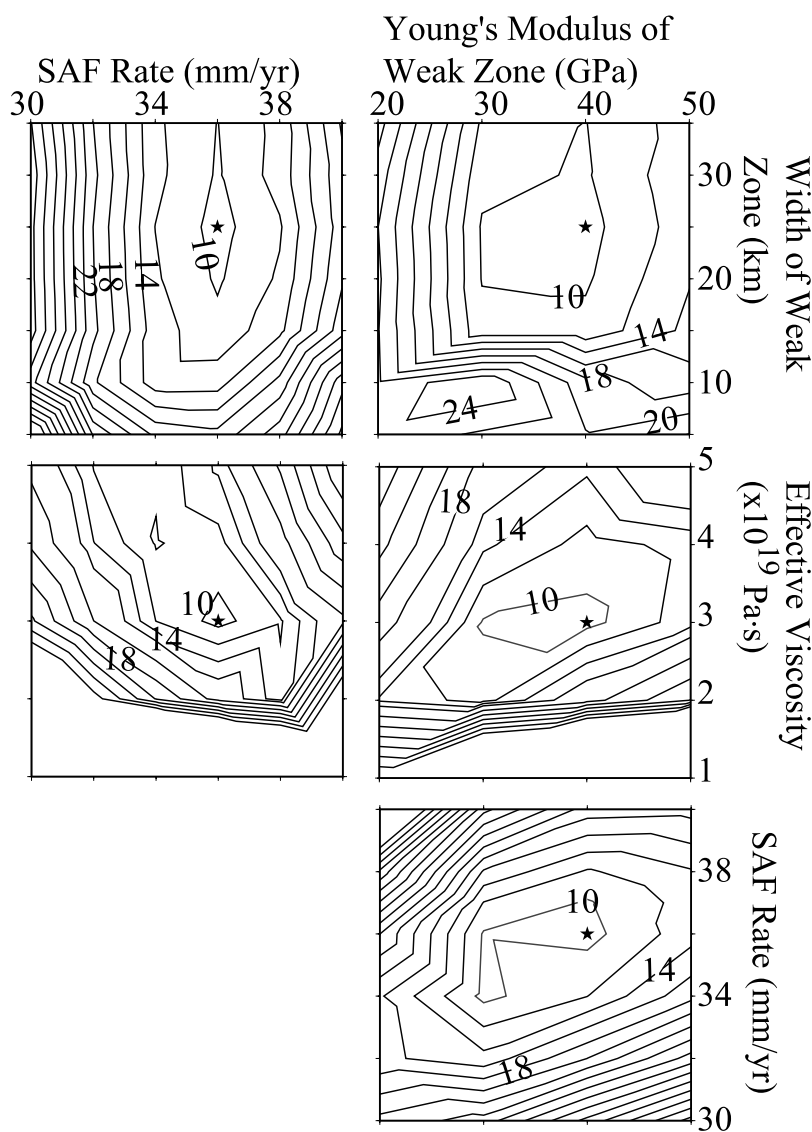


**Figure 18.** Contours of  $\chi^2$  misfit for case IVB (uniform elastic layer thickness, variable elastic properties, and variable rates for SAF and LAF. Parameters not shown are held to their best fit value (case IVB; Table 5). Star marks best fit values.  $\chi^2 \sim 18$  represents approximate 95% confidence level.

fault; hence results are not sensitive to rheologic variations far from the fault where stresses are low. Weak material near the fault (region of maximum strain accumulation) will deform by large amounts because stresses are high here. This may be why our models are not overly sensitive to the high rates of subsidence evidenced at some sites (e.g., 0613; FIBR; P807). These sites, located in a region of intense oil production, are all located more than 30 km from the SAF.

[48] Since our data and models constrain a minimum but not a maximum width of the weak zone, it may be preferable for future models to define this parameter with independent data (e.g., seismic data) and use the geodetic data to estimate its material properties. Ignoring such rheological complexity apparently does not induce significant bias in fault slip rate estimates based on the geodetic data, presumably because the rate estimate is mainly sensitive to the far-field rate, well-determined in this case by the GPS data. For example, ignoring lateral asymmetries and

fitting a simple elastic half-space model for two faults recovers a slip rate for the SAF (36 mm/yr, Table 4a) in excellent agreement with Holocene geologic estimates ( $34 \pm 3$  mm/yr, Table 1a). A finite element model with variable fault slip rates for the SAF and LAF, variable Young's modulus of a weak zone northeast of the fault, and variable viscosity below the upper crust yields the same rate,  $36^{+2}_{-1.5}$  mm/yr (Table 5), also equivalent within error to the Holocene average.

[49] However, ignoring the rheological complexity does affect estimates and interpretations of elastic layer thickness and locking depth (equated in our models). It has been known for some time that locking depth in the Carrizo segment is anomalously deep in elastic half-space models ( $\sim 20$ – $25$  km [e.g., Savage and Lisowski, 1998; Meade and Hager, 2005]). While our symmetric elastic half-space model yields a similar result (Figures 5a and 5b and Table 4a), the corresponding asymmetric model suggests

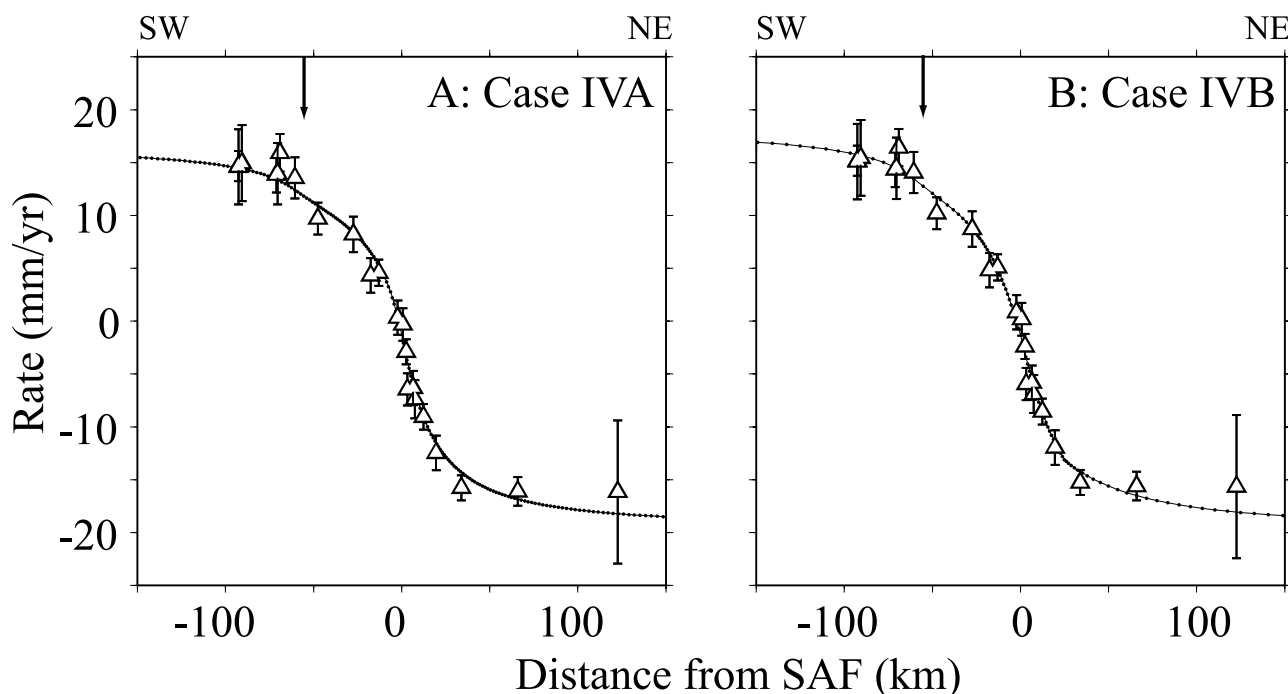


**Figure 19.** GPS data compared to best fit model for (a) case IVA (variable elastic layer thickness) and (b) case IVB (variable elastic properties), as well as variable LAF rate (arrow,  $x = -59$  km). Case IVB also has variable SAF rate ( $x = 0$ ). While both models fit the geodetic data, case IVB is our preferred model because it is also consistent with geologic, laboratory, paleoseismic, seismic and magnetotelluric data and is also the minimum misfit solution (Table 5).

that this may reflect an average of a thin (12 km) effective elastic thickness northeast of the fault and a thicker (38 km) effective elastic thickness southwest of the fault (Figures 5d and 5g and Table 4a). We believe that these parameter estimates are not physically meaningful; while such models fit the geodetic data, they are not consistent with the distribution of seismicity or major rock types in the region.

[50] Our results also provide information on the viscosity of the lower crust/upper mantle in this region. Most such viscosity estimates rely on postseismic response to past earthquakes. We suggest that interseismic strain accumulation data can also provide useful constraints to this parameter. The estimate is reasonably well constrained if independent information on elastic layer thickness and Young's modulus is available. For a reasonable range of these values, our models suggest viscosities in the range of  $2-5 \times 10^{19}$  Pa s. This should be interpreted as an average of lower crust and upper mantle values under the relatively low stress, low strain rate conditions that presumably characterize the SAF late in its earthquake cycle.

[51] Other faults in the region may influence the pattern of strain accumulation. Including the Los Alamos Fault in models significantly reduces misfit and improves the accuracy of the SAF rate estimate but does not have a significant impact on other parameter estimates (Table 5 and Figure 19).

[52] An important result from our work is that in the absence of seismic or other data that constrain material properties of the crust and upper mantle, interseismic GPS data may be able to provide some constraints on the rheology of the crust and upper mantle near active fault

zones. A combination of seismic and geodetic data is clearly preferable. In particular, seismic data provide key information on the dimensions of crustal units, reducing the nonuniqueness inherent to geodetic models of strain accumulation.

[53] **Acknowledgments.** This work was partially supported by NSF, NASA, and ONR grants to T.H.D., as well as a NASA Earth System Science Fellowship grant (NNG05GA83H) to G.S. We thank UNAVCO for assistance with the field observations. Many of the figures and maps were created with General Mapping Tools (GMT) by Pål Wessel and Walter H. F. Smith. The finite element meshes were generated using Gmsh by Christophe Geuzaine and Jean-Francois Remacle. We thank Pete La Femina, Dave Jackson, Shimon Wdowinski, Kevin Furlong, Chuck DeMets, Gregor Baechle, and Mark Grasmueck for insightful discussions and Duncan Agnew and Z.K. Shen for providing critical information on GPS site locations. We also thank two anonymous reviewers for very useful comments. Special thanks to the following people who allowed access to GPS stations: Jill Heeley, Joe Sills, Eric Stewart, Jim Stollberg, and Carl Loretta, and Rick Twisselman.

## References

- Altamimi, Z., P. Sillard, and C. Boucher (2002), ITRF2000: A new release of the International Terrestrial Reference Frame for earth science applications, *J. Geophys. Res.*, *107*(B10), 2214, doi:10.1029/2001JB000561.
- Atwater, T. (1970), Implications of plate tectonics for the Cenozoic tectonic evolution of western North America, *Geol. Soc. Am. Bull.*, *81*, 3513–3535.
- Balay, S., W. D. Gropp, L. C. McInnes, B. F. Smith, K. Buschelman, D. Kaushilk, V. Eijkhout, M. Knepley, and H. Zhang (2002), PETSc, Argonne Natl. Lab., Univ. of Chicago, Chicago, Ill.
- Crowell, J. C. (1952), Probable large lateral displacement on San Gabriel Fault, southern California, *Am. Assoc. Pet. Geol. Bull.*, *36*, 2026–2035.
- DeMets, C., and T. Dixon (1999), New kinematic models for Pacific-North America motion from 3 Ma to present: I. Evidence for steady motion and biases in the NUVEL-1A model, *Geophys. Res. Lett.*, *26*, 1921–1924.

- Dixon, T. H., A. L. Mao, M. Bursik, M. Heflin, J. Langbein, R. Stein, and F. Webb (1997), Continuous monitoring of surface deformation at Long Valley Caldera, California, with GPS, *J. Geophys. Res.*, *102*, 12,017–12,034.
- Dixon, T., F. Farina, C. DeMets, F. Suarez-Vidal, J. Fletcher, B. Marquez-Azua, M. Miller, O. Sanchez, and P. Umhoefer (2000), New Kinematic models for Pacific-North America motion from 3 Ma to present: II. Evidence for a “Baja California shear zone,” *Geophys. Res. Lett.*, *27*, 3961–3964.
- Dixon, T. H., E. Norabuena, and L. Hotaling (2003), Paleoseismology and Global Positioning System; earthquake-cycle effects and geodetic versus geologic fault slip rates in the eastern California shear zone, *Geology*, *31*, 55–58.
- Eberhart-Phillips, D., and A. J. Michael (1993), Three-dimensional velocity structure, seismicity, and fault structure in the Parkfield region, central California, *J. Geophys. Res.*, *98*, 15,737–15,758.
- Fay, N. P., and E. D. Humphreys (2005), Fault slip rates, effects of elastic heterogeneity on geodetic data, and the strength of the lower crust in the Salton Trough region, southern California, *J. Geophys. Res.*, *110*, B09401, doi:10.1029/2004JB003548.
- Fielding, E., R. G. Blom, and R. M. Goldstein (1998), Rapid subsidence over oil fields measured by SAR interferometry, *Geophys. Res. Lett.*, *25*, 3215–3218.
- Govers, R. (1993), Dynamics of lithospheric extension; a modeling study, Doctoral thesis, 240 pp., Univ. of Utrecht, Utrecht, Netherlands.
- Hager, B. H., G. A. Lyzenga, A. Donnellan, and D. Dong (1999), Reconciling rapid strain accumulation with deep seismogenic fault planes in the Ventura basin, California, *J. Geophys. Res.*, *104*, 25,207–25,219.
- Jackson, D. D., K. Aki, C. A. Cornell, J. H. Dieterich, T. L. Henyey, M. Mahdyiar, D. Schwartz, and S. N. Ward (1995), Seismic hazards in southern California—Probable earthquakes, 1994 to 2024, *Bull. Seismol. Soc. Am.*, *85*, 379–439.
- Jennings, C. W., and G. J. Saucedo (1994), Fault activity map of California and adjacent areas with locations and ages of recent volcanic eruptions, Calif. Div. of Mines and Geol., Sacramento.
- Kenner, S. J., and P. Segall (2000), Postseismic deformation following the 1906 San Francisco earthquake, *J. Geophys. Res.*, *105*, 13,195–13,209.
- Kenner, S. J., and P. Segall (2003), Lower crustal structure in northern California: Implications from strain rate variations following the 1906 San Francisco earthquake, *J. Geophys. Res.*, *108*(B1), 2011, doi:10.1029/2001JB000189.
- King, N. E., P. Segall, and W. H. Prescott (1987), Geodetic measurements near Parkfield, California, 1959–1984, *J. Geophys. Res.*, *92*, 2747–2766.
- Le Pichon, X., C. Kreemer, and N. Chamot-Rooke (2005), Asymmetry in elastic properties and the evolution of large continental strike-slip faults, *J. Geophys. Res.*, *110*, B03405, doi:10.1029/2004JB003343.
- Lisowski, M., J. C. Savage, and W. H. Prescott (1991), The velocity-field along the San Andreas Fault in central and southern California, *J. Geophys. Res.*, *96*, 8369–8389.
- Malservisi, R., K. P. Furlong, and T. H. Dixon (2001), Influence of the earthquake cycle and lithospheric rheology on the dynamics of the eastern California shear zone, *Geophys. Res. Lett.*, *28*, 2731–2734.
- Malservisi, R., C. Gans, and K. P. Furlong (2003), Numerical modeling of strike-slip creeping faults and implications for the Hayward Fault, California, *Tectonophysics*, *361*, 121–137.
- Mao, A. L., C. G. A. Harrison, and T. H. Dixon (1999), Noise in GPS coordinate time series, *J. Geophys. Res.*, *104*, 2797–2816.
- McMeeking, R. M., and J. R. Rice (1975), Finite element formulation for problems of large elastic-plastic deformation, *Int. J. Solid Struct.*, *11*, 601–616.
- Meade, B. J., and B. H. Hager (2005), Block models of crustal motion in southern California constrained by GPS measurements, *J. Geophys. Res.*, *110*, B03403, doi:10.1029/2004JB003209.
- Melosh, H. J., and A. Raefsky (1980), The dynamical origin of subduction zone topography, *Geophys. J. R. Astron. Soc.*, *60*, 333–354.
- Melosh, H. J., and A. Raefsky (1981), A simple and efficient method for introducing faults into finite element computations, *Bull. Seismol. Soc. Am.*, *71*, 1391–1400.
- Norabuena, E., et al. (2004), Geodetic and seismic constraints on some seismogenic zone processes in Costa Rica, *J. Geophys. Res.*, *109*, B11403, doi:10.1029/2003JB002931.
- Nur, A., and G. Mavko (1974), Postseismic viscoelastic rebound, *Science*, *183*, 204–206.
- Page, B. M. (1981), *The Southern Coast Ranges*, Prentice-Hall, Upper Saddle River, N. J.
- Powell, R. E., and R. J. Weldon (1992), Evolution of the San-Andreas Fault, *Annu. Rev. Earth Planet. Sci.*, *20*, 431–468.
- Rybicki, K. (1971), The elastic residual field of a very long strike-slip fault in the presence of a discontinuity, *Bull. Seismol. Soc. Am.*, *61*, 79–92.
- Rybicki, K., and K. Kasahara (1977), A strike-slip fault in a laterally inhomogeneous medium, *Tectonophysics*, *42*, 127–138.
- Savage, J. C. (1980), *Dislocations in Seismology*, Elsevier, New York.
- Savage, J. C., and R. O. Burford (1973), Geodetic determination of relative plate motion in central California, *J. Geophys. Res.*, *78*, 832–845.
- Savage, J. C., and M. Lisowski (1998), Viscoelastic coupling model of the San Andreas Fault along the Big Bend, southern California, *J. Geophys. Res.*, *103*, 7281–7292.
- Savage, J. C., and W. H. Prescott (1978), Asthenosphere readjustment and the earthquake cycle, *J. Geophys. Res.*, *83*, 3369–3376.
- Segall, P. (2002), Integrating geologic and geodetic estimates of slip rate on the San Andreas Fault system, *Int. Geol. Rev.*, *44*, 62–82.
- Sella, G. F., T. H. Dixon, and A. Mao (2002), REVEL: A model for Recent plate velocities from space geodesy, *J. Geophys. Res.*, *107*(B4), 2081, doi:10.1029/2000JB000033.
- Shapiro, N. M., M. Campillo, L. Stehly, and M. H. Ritzwoller (2005), High-resolution surface-wave tomography from ambient seismic noise, *Science*, *307*, 1615–1618.
- Sibson, R. H. (1983), Continental fault structure and the shallow earthquake source, *J. Geol. Soc. London*, *140*, 741–767.
- Sieh, K. E., and R. H. Jahns (1984), Holocene activity of the San Andreas Fault at Wallace Creek, California, *Geol. Soc. Am. Bull.*, *95*, 883–896.
- Stein, S., and R. G. Gordon (1984), Statistical tests of additional plate boundaries from plate motion inversions, *Earth Planet. Sci. Lett.*, *69*, 401–412.
- Stein, S., and M. Wysession (2003), *An introduction to Seismology, Earthquakes, and Earth Structure*, 1st ed., 498 pp., Blackwell, Malden, Mass.
- Thatcher, W. (1983), Nonlinear strain buildup and earthquake cycle on the San Andreas Fault, *J. Geophys. Res.*, *88*, 5893–5902.
- Turcotte, D. L., and G. Schubert (2002), *Geodynamics*, 2 ed., 456 pp., Cambridge Univ. Press, New York.
- Unsworth, M., and P. A. Bedrosian (2004), Electrical resistivity structure at the SAFOD site from magnetotelluric exploration, *Geophys. Res. Lett.*, *31*, L12S05, doi:10.1029/2003GL019405.
- Ward, S. N. (1990), Pacific-North America plate motions: New results from very long base-line interferometry, *J. Geophys. Res.*, *95*, 21,965–21,981.
- Weertman, J., and J. R. Weertman (1964), *Elementary Dislocation Theory*, 232 pp., Oxford Univ. Press, New York.
- Xu, H., J. Dvorkin, and A. Nur (2001), Linking oil production to surface subsidence from satellite radar interferometry, *Geophys. Res. Lett.*, *28*, 1307–1310.
- Zumberge, J. F., M. B. Heflin, D. C. Jefferson, M. M. Watkins, and F. H. Webb (1997), Precise point positioning for the efficient and robust analysis of GPS data from large networks, *J. Geophys. Res.*, *102*, 5005–5017.

T. Dixon and G. Schmalzle, Rosenstiel School of Marine and Atmospheric Sciences, University of Miami, Miami, FL 33149, USA. (gschmalzle@rsmas.miami.edu)

R. Govers, Faculty of Earth Sciences, Utrecht University, P.O. Box 80.021, NL-3508 TA, Utrecht, Netherlands.

R. Malservisi, Department of Earth and Environmental Sciences, Ludwig-Maximilians University, D-80333, Munich, Germany.